Nanoscale

ROYAL SOCIETY OF CHEMISTRY

PAPER

View Article Online
View Journal | View Issue



Cite this: *Nanoscale*, 2025, **17**, 16256

# Upholding hyaluronic acid's multi-functionality for nucleic acid drug delivery to target EMT in breast cancer†

Lorenz Isert,[a] Irene Gialdini,[b] Thi My Hanh Ngo,[a] Gabriele Loiudice,[a] Don C. Lamb[b,c] and Olivia M. Merkel*[a,c]

Received 23rd February 2025,
Accepted 2nd June 2025

DOI: 10.1039/d5nr00808e

rsc.li/nanoscale

Synthetic nanoparticles can stably encapsulate nucleic acids as active pharmaceutical payloads. Recently, mRNA- and siRNA-based medicines have been successfully approved for preventing or treating infectious or orphan diseases. RNA interference is particularly relevant for cancer therapy, as tumors often involve up- or dys-regulated proteins that drive malignancy. This study aimed to develop a nanoparticulate delivery vehicle that targets EMT-phenotypic breast cancer cells, which lack effective treatment options. These "undruggable" tumors may be addressed by nanoparticles that target EMT-specific cell surface receptors. CD44, a transmembrane protein linked to cancer malignancy and EMT, was identified as a promising candidate. This work investigated the use of hyaluronic acid (HA) in HA-modified polyelectrolyte complexes (polyplexes, Px) for its dual roles as a targeting ligand and a stabilizing stealth-molecule. Various strategies for non-covalently immobilizing HA on the particle surfaces were tested. HAPx nanoparticles demonstrated HA : PEI-ratio dependent stability against competing anionic biomolecules, improved colloidal stability in protein-rich environments mimicking *in vivo* conditions, and enhanced selectivity and efficacy in targeting E/M-hybrids and EMT-positive cells *via* CD44-HA mediated endocytosis. Finally, our results indicate different internalization kinetics and efficiencies between CD44v and CD44s isotypes, highlighting the need to consider CD44 heterogeneities in the clinical development of HA-based drug delivery systems.



## Introduction

Modern drug delivery with nanoparticulate formulations such as liposomes (*e.g.* Doxil®), lipid-based nanoparticles (LNPs), polymer–drug conjugates, polymeric nanoparticles (micelles, polyplexes), or inorganic nanoparticles exploits two major conditions for successful cancer treatment.[1] First, passive targeting based on the enhanced permeability and retention (EPR) effect. EPR arises from the leaky endothelium and poor lymphatic clearance within the tumor tissue, and enables the accumulation of the nanomedicine at the tumor site.[2] Second, ligand-mediated targeting *via* ligand immobilization on the particle surface, providing nano-formulations with cell-receptor selectivity. Due to overexpression of surface proteins in many cancers, unique nanoparticle-cancer cell interaction profiles can be specifically established by choosing the right targeting moiety for the respective tumor.[2,3] However, the mode of ligand presentation (density, coupling chemistry *vs.* non-covalent modification), the ligand–receptor affinity and the absolute receptor quantity and recycling rates are crucial factors for efficient receptor-mediated endocytosis and require careful nanocarrier design.[3–7] Additionally, the physico-chemical properties of a drug delivery system, defined by the carrier and its cargo, may alter upon systemic administration as a result of interactions with the non-targeted biomolecules. Hence, the particle's fate and the therapeutic efficacy strongly rely on the quantity and type of biomolecules bound to the nanocarrier surface as they promote systemic clearance, on/off-tissue accumulation and receptor–ligand interaction, emphasizing the need for rigorous choice of the nanocarrier design.[8]

The naturally occurring glycosaminoglycan hyaluronic acid (HA) offers a multitude of features that are desirable and required for the clinical use of nanomedicines, such as its biocompatibility, biodegradability and biosafety. In addition, the endogenously expressed hyaladherins, *i.e.* hyaluronan-binding

[a]*Department of Pharmacy, Ludwig-Maximilians-Universität München, Butenandtstraße 5, 81377 Munich, Germany*
[b]*Department of Chemistry, Ludwig-Maximilians-Universität München, Butenandtstraße 5, 81377 Munich, Germany*
[c]*Center for NanoScience (CeNS), Ludwig-Maximilians-Universität München, 80799 Munich, Germany. E-mail: Olivia.merkel@lmu.de*
† Electronic supplementary information (ESI) available. See DOI: https://doi.org/10.1039/d5nr00808e

proteins (CD44, RHAMM, HARE, LYVE-1), allow HA-decorated drug delivery systems to be internalized *via* receptor-mediated endocytosis.[9,10] HARE and LYVE-1 receptors are considered to be detrimental for the clinical implementation of HA-functionalized drugs as they promote hepatic and lymphatic clearance, respectively.[9,11] Conversely, the CD44 receptor is a promising candidate due to their cancer-specific overexpression in many types of tissues.[12–14] The low molecular weight standard isoform of CD44 (~85 kDa, CD44s) is ubiquitously expressed in normal and cancer cells, but often correlates in expression with cancer conferring stem-like properties.[15] Additionally, nine higher molecular weight variant isoforms (CD44v) are known, which contain a variable number of exon insertions (v1–v10) coding for peptides located in the juxta membrane ectodomain.[16] Notably, the expression of the variant CD44v isoforms is mainly restricted to cancer cells[17,18] which was recently exploited for the design of novel anti-cancer therapies.[16,18,19]

The epithelial-to-mesenchymal transition (EMT) is a dynamic differentiation process that cancer cells exploit to disseminate from the primary tumor site and to invade into and through the stromal compartment.[20,21] A hallmark of the transition comprises the downregulation of E-cadherin (CDH1),[22] the responsible surface protein for establishing adherens junctions that define the strengths of cell–cell contacts.[23,24] In breast cancer, disease malignancy correlates with EMT, which in turn correlates with overexpression of CD44. More precisely, it was found that the total expression and the relative abundance of CD44s and CD44v isoforms dynamically vary depending on tumor grade and cellular differentiation.[25,26] Since the phenomenon of EMT is thought to be spatially restricted to the tumor-stromal boundary,[27,28] EMT-specific cell surface markers such as CD44s/v hold great promise for targeted drug delivery, in particular for nanomedicines, which are prone to interact with surface receptors at the tumor margin but do not passively penetrate the tumor.[29,30] Thus, the heterogeneity of CD44 isotypes that occurs at different EMT-stages may ultimately govern the therapeutic efficiency of HA-presenting nanocarriers. Combining the CD44-targeting approach with the silencing of biomolecules responsible for EMT could be a powerful strategy to prevent cancer progression or even metastasis whilst avoiding off-target cytotoxicity. Finally, targeting cancer cells *via* the CD44 receptor offers a possible therapeutic strategy to tackle the otherwise "undruggable" nature of triple-negative breast cancer, which is frequently linked to an EMT-positive phenotype.[31]

In this study, branched, high-molecular weight poly(ethylenimine) (PEI) was used as a gold standard polymer nanocarrier for siRNA to evaluate the properties of HA-coated nanoparticles for drug delivery in the context of breast cancer. This work particularly emphasises the targetability of cancer-associated EMT stages, with a focus on receptor isoform expression and nanoparticulate formulation strategies. The polycation PEI efficiently condenses negative siRNA molecules to form polyplexes (Px) that bear a cationic zeta potential. Most carboxyl-groups within the HA polymer are deprotonated at physiological pH,[32] allowing for electrostatic adsorption on positively charged Px (HAPx). Here, three distinct strategies for non-covalently immobilizing HA on Px are presented, and their overall impact on the resulting physico-chemical properties, stability and cellular *in vitro* performance are discussed. The uptake and kinetics of the distinct nanoparticles were evaluated with the use of well-selected breast cancer cell lines, to discriminate between CD44s and CD44v isoform-mediated mechanisms. Finally, superior efficacy of optimized HA-coated PEI formulation is assessed *in vitro* in a siRNA-mediated therapeutic gene silencing approach.

## Material & methods

### Materials and cell culture

Branched Poly(ethyleneimine) (PEI) $M_n$ = 10 kDa (408727), HEPES (4-(2-hydroxyethyl)-1-piperazineethanesulfonic acid), heparin sodium salt, formaldehyde solution (≥36%), 4′,6-diamidino-2-phenylindole dihydrochloride (DAPI), FluorSave reagent, DNase I (recombinant, RNase-free), cOmplete™, EDTA-free protease inhibitor cocktail, phosphatase inhibitor cocktail 2, RIPA buffer, Tris buffered saline powder, Ponceau S Stain, Tween 20, Amersham™ Protran® western-blotting-membrane (nitrocellulose) and for cell culture Eagle's minimum essential medium (EMEM), RPMI-1640 medium, Dulbecco's modified eagle's medium (DMEM), fetal bovine serum (FBS), penicillin–streptomycin (Pen/Strep) solution, Dulbecco's phosphate buffered saline (PBS), trypsin-EDTA solution 0.05% and 0.25%, 200 mM of L-glutamine solution, and dimethyl sulfoxide (DMSO) were obtained from Sigma-Aldrich (Taufkirchen, Germany). GAPDH Monoclonal Antibody (ZG003), Green Pierce™ BCA Protein Assay Kit, Lipofectamine2000, Novex™ 10% Tris-glycine mini gels (WedgeWell™ format, 15-well), Novex™ Value™ 4–20% Tris-glycine mini gels (1.0 mm, 10-well), Page Ruler™ Plus prestained protein ladder 10 to 250 kDa, Tris glycin transfer buffer, SuperSignal™ West Pico PLUS chemiluminescent substrate, rhodamine phalloidin, high capacity cDNA synthesis kit, Power SYBR™ Green PCR master mix, PureLink™ RNA mini kit and for cell culture Leibovitz's L-15 medium and MEM non-essential amino acids solution (100×) were purchased from Thermo Fisher Scientific (Darmstadt, Germany). Hs_GAPDH_1_SG QuantiTect primer assay (QT00079247) and Hs_XBP1_1_SG QuantiTect primer assay (QT00068383) were obtained from Qiagen (Hilden, Germany). Rotiphorese 10× SDS Page, Rotilabo®-blotting papers and methanol (blotting grade) were purchased from Carl Roth (Karlsruhe, Germany). rh-TGF-β 1 (transforming growth factor beta 1) and rh-EGF (epidermal growth factor) were bought from ImmunoTools (Friesoythe, Germany). Laemmli loading buffer (4×) and round glass coverslips ($\phi$ 13 mm) were purchased from VWR (Allison Park, PA, USA). Alexa Fluor® 488 anti-human CD44 antibody (103015) and Alexa Fluor® 488 isotype control antibody (400625) were purchased from Biolegend (San Diego, CA, USA). Human CD44s pan specific antibody and Hyaluronan (HA) (medium MW;

119 kDa; GLR004; LOT: 1580675) were bought from R&D systems (Minneapolis, MN, USA). Amine-modified eGFP siRNA (5′-pACCCUGAAGUUCAUCUGCACCACcg, 3′-ACUGGGACUUCAAGUAGACGGGUGGC), and scrambled siRNA (5′-pCGUUAAUCGCGUAUAAUACGCGUat, 3′-CAGCAAUUAGCGCAUAUUAUGCGCAUAp) were purchased from Integrated DNA Technologies (Leuven, Belgium). Anti-XBP1 antibody (ab37152) was purchased from Abcam (Cambridge, UK). HyClone trypan blue solution 0.4% in phosphate-buffered saline was obtained from FisherScientific (Hampton, NH, USA). E-cadherin Antibody (G-10) and mouse IgG kappa binding protein (m-IgGκ BP) conjugated to horseradish peroxidase (HRP) (sc-516102) were ordered from Santa Cruz Biotechnology (Dallas, Texas, USA). XBP1 siRNA (5′-CACCCUGAAUUCAUUGUCU[dT][dT], 3-AGACAAUGAAUUCAGGGUG[dT][dT]) was obtained from Qiagen (Hilden, Germany) based on a publication by Chen *et al.*[33]

MCF7 luminal A breast cancer cells were cultured in EMEM supplemented with 10% FBS, 1× Pen/Strep, 1× MEM non-essential amino acids solution and 2 mM glutamine. The HER2-positive breast cancer cell line HCC1954 was grown in RPMI-1640 medium supplemented with 10% FBS and 1× Pen/Strep. MDA-MB-231 triple negative breast cancer (TNBC) cells were cultured in high glucose (4500 mg $L^{-1}$) DMEM. 10% FBS, 1× Pen/Strep and 2 mM glutamine were added to the medium. The latter three cell lines were cultured in a humidified atmosphere with 5% $CO_2$ at 37 °C. The second TNBC cell line MDA-MB-468 was grown in L-15 medium supplemented with 20% FBS, 2 mM glutamine and 1× Pen/Strep in a humidified incubator with 0% $CO_2$ at 37 °C.

## Preparation and characterization of polyplexes

**Hyaluronic acid-coating of polyplexes.** Three different approaches were evaluated to nanoprecipitate anionic hyaluronic acid (HA) on the surface of positively charged PEI Px. The indicated HA : PEI ratios (1 : 10, 1 : 5, 1 : 2.5, 1 : 1, 2.5 : 1, 5 : 1, and 10 : 1) depict weight ratios. The implemented amounts of PEI and siRNA were based on optimized standard PEI Px at an N/P-ratio (nitrogen-to-phosphate ratio) of 5 with 100 pmol of siRNA and were kept constant throughout the different procedures. siRNA and HA stock solutions were dissolved in RNAase-free water, whereas PEI was dissolved in sterile-filtered 10 mM HEPES at pH 7.4. Subsequent dilutions were made in sterile-filtered 10 mM HEPES at pH 7.4:

(1) "2-step coating" (Fig. 1a): in the first step, PEI-siRNA core Px-intermediates were produced as commonly described. In short, the PEI solution was mixed with 100 pmol of siRNA (volumes 1 : 1) by gently pipetting up and down to form PEI Px during a 20 min incubation step. In order to obtain HA-coated

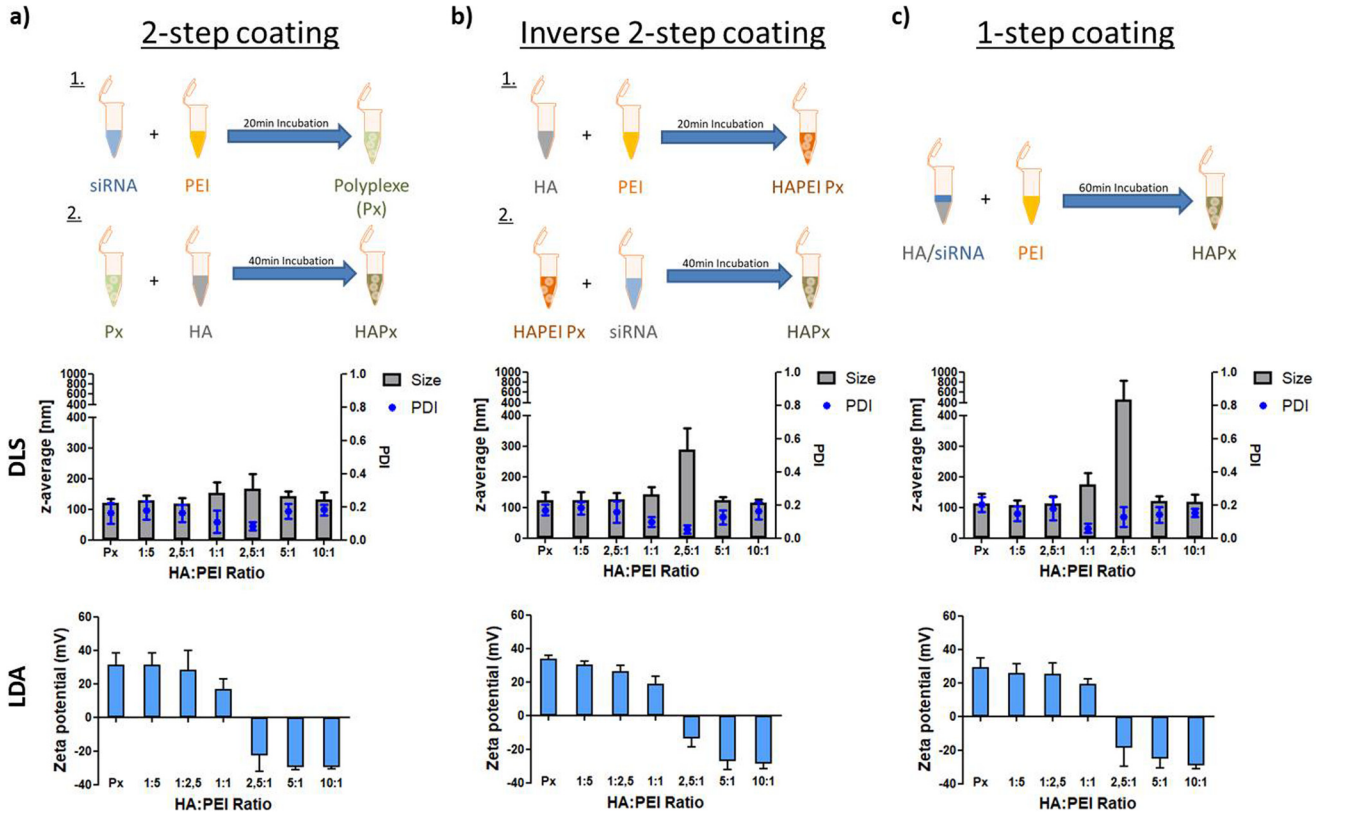


**Fig. 1** Physico-chemical characterization of Px produced *via* (a) 2-step coating (b) inverse 2-step coating and (c) 1-step coating depending on the HA : PEI ratio ($n$ = 3). The upper panel shows a scheme that summarizes the particle preparation protocols. The central panel depicts the particles' hydrodynamic diameter (shown as $z$-average, left $y$-axis) and polydispersity index (PDI, right $y$-axis). The lower panel displays the zeta potentials of the respective particles. The error bars represent standard deviation ($n$ = 4).

 

Px (HAPx) the Px containing suspension was transferred into another Eppendorf tube containing HA solutions (V(HA) = 15% of Px volume) of varying concentrations, and mixtures were incubated for another 40 min.

(2) "Inverse 2-step coating" (Fig. 1b): in the first step, PEI-HA core Px were produced. Briefly, the PEI solution was mixed with varying amounts of HA (volumes 1 : 1) by gently pipetting up and down. After 20 min of incubation, Px of different HA : PEI-ratios were transferred into Eppendorf tubes containing 100 pmol of siRNA (V(siRNA) = 15% of Px volume) which were incubated for another 40 min allowing for maximum complexation.

(3) "1-step-coating" (Fig. 1c): the PEI solution and the anionic components (HA and siRNA) were mixed in one single step. In brief, 100 pmol of siRNA was combined with varying amounts of HA (1 : 10 to 10 : 1) in the same tube. Subsequently, the HA/siRNA-blend was mixed with the PEI solution (1 : 1) to form HAPx during 60 min of incubation.

The final volume of colloidal (HA)Px solution was kept constant for all three procedures.

**Dynamic light scattering (DLS) and laser Doppler anemometry (LDA).** The Zetasizer nano ZS (Malvern Instruments, Malvern, UK) was used to measure hydrodynamic size (*z*-average), polydispersity index (PDI) and ζ-potential of the aforementioned Px formulations. To assess particle sizes and PDIs, 100 μL of freshly prepared (HA)Px were added to a disposable cuvette and measured by DLS at 173° backscatter with three automatic scan cycles. For the measurement of ζ-potential, the 100 μL of Px were recovered and carefully redispersed in 600 μL of 10 mM HEPES pH 7.4. The 7× dilution was filled into a zeta cell (Zeta Sizer series, Malvern, UK) and measured by LDA. Results are shown as mean ± SD ($n$ = 3).

For the long-term storage study, Px were prepared in 10 mM HEPES pH 7.4 as described above using the 3 coating methods, aliquoted and stored at room temperature (RT) under exclusion of light. DLS measurements were performed at 0 h, 24 h, 48 h, 72 h, 96 h, 168 h (1 week), 336 h (2 weeks), 672 h (4 weeks) and 1008 h (6 weeks), respectively.

**SYBR gold assay – encapsulation of siRNA.** To completely encapsulate siRNA within Px, generally an excess of PEI (here: N/P-ratio of 5) is used. However, co-encapsulation of HA and siRNA within one particle may electrostatically and sterically impair siRNA encapsulation. To clarify whether siRNA is released from the nanoparticles during the coating process, the SYBR Gold Assay was used 34. HAPx of different HA : PEI ratios (w/w) were prepared in HEPES 10 mM (pH 7.4). Subsequently, 100 μL of each Px suspension was distributed in a white FluoroNunc 96-well plate (FisherScientific, Hampton, NH, USA). A 4X SYBR Gold solution (30 μL) was added to each well, and the plate was incubated for 10 min in the dark. A fluorescence plate reader (Tecan SPARK, Tecan, Männedorf, Switzerland) was utilized to determine the fluorescence intensity of the different ratios ($\lambda_{Ex}$ = 492 nm; $\lambda_{Em}$ = 555 nm). Free siRNA served as 100% reference value. Measurements were carried out in triplicates, and the results were shown as mean value ± SD ($n$ = 2).

**Heparin/SYBR gold competition assay – polyplex stability over polyanions.** Polyplex assembly results in a compaction of siRNA and cationic polymer molecules. In the case of fluorescently labeled siRNA, the fluorescent entities tend to converge in a way that causes self-quenching of the dye upon excitation, leading to a decrease in the overall fluorescence intensity.[34] This phenomenon was exploited to monitor polyplex compaction and de-compaction. Hence, one can investigate colloidal stability of particles *via* de-quenching, which indicates particle disassembly. Here, amine-modified siRNA was labeled with succinimidyl ester (NHS) modified Alexa Fluor 647 (AF647) (Life Technologies, Carlsbad, California, USA) following the manufacturer's protocol. (HA)Px particles were prepared with 100 pmol of AF647-labeled siRNA as described above. For each particle suspension, 10 μL per samples were pipetted in white FluoroNunc 96-well plates and subsequently filled up to a total volume of 100 μL to reach experimental conditions. Colloidal stability was assessed for three different conditions: dispersed in 10 mM HEPES pH 7.4 (standard buffer), 10% FBS (*in vitro*-like) and 90% FBS (*in vivo*-like). Fluorescence intensity was determined at intervals of 15 min for 4 h with a fluorescence plate reader ($\lambda_{Ex}$ = 630 nm; $\lambda_{Em}$ = 680 nm). For the 100% reference value, 10 pmol of free A647 siRNA diluted in 100 μL of the respective medium was used. The time-dependent fluorescence intensities were always related to the respective value of free AF647 siRNA. The relative fluorescence normalized to free siRNA is calculated as:

$$\text{Rel. fluorescence} = \frac{\text{fluorescence of particles at } t(x)}{\text{fluorescence of free siRNA at } t(x)} \leq 1.0.$$

Measurements were performed in triplicate, and the results are shown as mean value ± SD.

**Fluorescence correlation spectroscopy (FCS) – polyplex stability over serum proteins.** If not otherwise stated, Px and 2-step-coated HAPx (HA to PEI ratio of 2.5 to 1) were prepared as described above with a 25/27mer negative control siRNAs, 15% of which were labeled with ATTO643. For the FCS measurements, the nanoparticle preparations were diluted 1 : 10 in HEPES, 10% or 90% FBS. As controls, 5 nM ATTO643 and 25 nM siRNA-ATTO643 solutions were prepared in HEPES, 10% or 90% FBS. For each diluted sample, 20–30 μL were added to a well of an 8-well LabTek I slide (VWR) previously passivated with 1% Tween20 to prevent adsorption of the labeled material to the glass surface. The FCS measurements were performed on a home-built confocal microscope as described elsewhere[35] using a pulsed diode laser of 635 nm wavelength (LDH-P-C-635M, PicoQuant) at a laser power of 2 μW before the objective and a 60× water immersion objective (Plan Apo 60× WI/NA 1.27, Nikon). The fluorescence emission was separated from the excitation pathway with a quad-line 405/488/561/635 beamsplitter (Semrock), spectrally filtered with a 635 nm longpass (AHF) emission filter and then detected with an avalanche photodiode (APD) detector (Count® single photon counting module, laser components). Excitation and emission were synchronized *via* time-correlated single-photon counting (TCSPC, SPC-150 Becker and Hickl) electronics. The alignment

of the system was routinely checked by measuring an aqueous solution of ATTO655 with FCS. The correlation analyses were performed with PIE Analysis in MATLAB (PAM)[36] and the autocorrelation functions (ACFs) were fit with a diffusion model with up to three-components depending on the sample, assuming a 3D Gaussian focus shape:

$$G(\tau) = \frac{\gamma}{(A_1 + A_2 + A_3)^2}\left\{\left[A_1\left(1+\frac{4D_1\tau}{\omega_r^2}\right)^{-1}\left(1+\frac{4D_1\tau}{\omega_z^2}\right)^{-\frac{1}{2}}\right] + \left[A_2\left(1+\frac{4D_2\tau}{\omega_r^2}\right)^{-1}\left(1+\frac{4D_2\tau}{\omega_z^2}\right)^{-\frac{1}{2}}\right] + \left[A_3\left(1+\frac{4D_3\tau}{\omega_r^2}\right)^{-1}\left(1+\frac{4D_3\tau}{\omega_z^2}\right)^{-\frac{1}{2}}\right].$$

Here, $\tau$ represents the time delay of the correlation, $D_i$ the diffusion coefficient of the species $i$ and $\omega_r$ and $\omega_z$ indicate the lateral and axial focus sizes, respectively. The shape factor $\gamma$ is $2^{-3/2}$ for a 3D Gaussian focus. $A_i$ represents the relative amplitude of the corresponding fluorescent species in the observation volume. It should be noted that, in this model, all the components are assumed to have equal brightness. However, if an accurate quantification of $A_i$ is desired, the relative brightness of each species needs to be included in the analyses.[37]

### *In vitro* evaluation of HA-coated polyplexes in four breast cancer cell lines

**Immunostaining/flow cytometry – cell surface expression of CD44 receptor (CD44-R) in breast cancer.** For each experiment, 50.000 cells of MCF7, HCC1954, MDA-MB-468 and MDA-MB-231 cell lines were seeded in triplicates in a 24-well plate. After 48 h, cells were washed 3× with sterile PBS and harvested. Subsequently, cells were centrifuged at 400*g* for 5 min, and the supernatant was discarded. In the next step, 100 000 cells of each cell line were re-dispersed in 50 μL of PBS containing 2 μg ml$^{-1}$ of AF488-labeled CD44-R-specific or isotype control antibody, respectively. Blank samples were treated with neither antibody. After 30 min of incubation at 4 °C, 1 ml of PBS was added, cells were vortexed, centrifuged and the supernatant was removed. Following an additional washing step, cells were re-suspended in 400 μL of PBS with 2 mM EDTA, and samples were analyzed using an Attune® NxT flow cytometer (Thermo Fisher Scientific) with 488 nm excitation and 530/30 emission filter. All cells were gated according to morphology based on forward/sideward scattering, and 10.000 gated events were evaluated per sample. Results are shown as mean ± SD ($n$ = 2).

To test for CD44-R expression upon EMT induction, 50.000 cells of MCF7, HCC1954 and MDA-MB-468 cell line were incubated for 48 h in 10 ng ml$^{-1}$ TGF-β1 and 50 ng ml$^{-1}$ EGF containing medium, respectively. Afterwards receptor expression was measured as described above. Results are shown as mean ± SD ($n$ = 2).

**Flow cytometry – cellular uptake of HAPx depending on cell line and coating procedure.** For each cell line, 50 000 cells were seeded in duplicates in a 24-well plate. After 24 h, cells were washed with PBS and transfected with 100 μL of freshly prepared polyplexes (Px and HAPx (1 : 10 to 10 : 1)) containing 100 pmol AF488-siRNA in 400 μL of the respective medium. After 0.25, 1, or 4 h incubation, medium in the wells was filled up to 1 ml. After another 0.75, 3, or 20 h of incubation, respectively, cells were washed 3× times with PBS and harvested. Centrifuged cell pellets were re-suspended in 500 μL of PBS with 2 mM EDTA, and particle uptake was analyzed using an Attune® NxT flow cytometer with 488 nm excitation and 530/30 emission filter. Forward/sideward scatter and laser intensity were kept the same for all the cell lines and time points to allow for comparison of intercellular nanoparticle endocytosis. Results are shown as mean ± SD ($n$ = 2).

**Confocal scanning microscopy – intracellular fate of polyplexes.** Confocal microscopy and image analysis was used to assess and quantify co-localization of Px within lysosomes after cellular internalization. Briefly, sterile glass coverslips were distributed in a 24-well plate. Thereafter, 50.000 cells were seeded to attach for 24 h. Px were prepared with AF647-labeled siRNA as described above, and cells were transfected for 24 h. During the last hour of transfection, media was supplemented with LysoTracker™ Green DND-26 (invitrogen) lysosomal stain according to the manufacturer's protocol. Hereinafter, wells were washed 3 times with PBS before cells were fixed for 15 min with a 4% formaldehyde solution. Cells were washed another 3 times with PBS. Nuclear staining was achieved by 10 min incubation with a 0.5 μg ml$^{-1}$ DAPI solution. Finally, after an additional washing step, samples were mounted on glass slides using FluorSave and stored at 4 °C until the next day. Fluorescence images were acquired using a laser scanning microscope (Leica SP8 inverted, Software: LAS X, Leica microsystems GmbH, Wetzlar, Germany) equipped with an HC PL APO CS2 40×/1.30 and 63×/1.40 oil immersion objective. Diode lasers (405 nm and 638 nm) and a semiconductor laser OPSL (488 nm) were chosen for excitation, emission of blue (PMT1: 410 nm–488 nm), green (HyD3: 495 nm–625 nm) and red (PMT2: 643 nm–785 nm) dyes, was detected respectively. Images were further processed with the JACoP plug-in of Fiji image analysis software.[38] For the co-localization analysis of each HAPx species, at least 4 cells of 3 samples were manually outlined to reduce background noise. Thresholds of the green and red channel were manually adjusted and kept constant within the respective cell line. One-way ANOVA with Dunnett's multiple comparison test was performed in GraphPad prism software to calculate $p$-values at 95% confidence interval.

**RT-qPCR – XBP1 knockdown in MDA-MB-231 cells.** For the gene silencing experiment, 24 h prior to transfection 200.000 MDA-MB-231 cells were seeded in a 6-well-plate and incubated until the next day. Cells were transfected with 100 μL of Px or HAPx polyplexes produced by "2-step coating" and containing 100 pmol of XBP1 or scrambled siRNA. Positive controls consisted of Lipofectamine2000 lipoplexes while negative controls consisted of blank/untreated cells. After 24 h, cells were harvested and processed to isolate total RNA using the PureLink

 

RNA mini kit according to the manufacturer's protocol (Life Technologies, Carlsbad, California, USA). cDNA was synthetized from total RNA using the high-capacity cDNA synthesis kit (Applied Biosystems, Waltham, Massachusetts, USA). Afterwards, the obtained cDNA was diluted 1 : 10 and a qPCR was performed using the SYBR™ Green PCR Master Mix (Thermo Fisher Scientific) with primers for human GAPDH (Qiagen, Hilden Germany) for normalization. Cycle thresholds were acquired by auto setting within the qPCRsoft software (Analytic Jena AG, Jena, Germany). Values are given as mean ± SD.

### Western blotting

Protein levels of CDH1, XBP1, CD44s and CD44v in the four cell lines were analyzed *via* western blotting. Of each cell line, 300 000 cells were seeded in triplicates in a 6-well plate and cultured for 24 h. Total protein extract was isolated after incubation. Briefly, cells were washed 3 times with PBS prior to cell lysis. To each well, 70 μL of proteinase- and phosphatase-inhibitor containing RIPA buffer was added, and cells were kept on ice for 30 min. Hereinafter, wells were thoroughly scraped, and the extracts were transferred into 1.5 ml Eppendorf tubes. After a 10 min centrifugation step at 4 °C, total protein concentration was assessed according to the manufacturer's protocol (Pierce™ BCA protein assay kit). For protein extraction of the transcription factor XBP1, the "nuclear extraction kit" was utilized according to the manufacturer's protocol (Abcam, Cambridge, UK). Gels were loaded with 30 μg protein per sample, and electrophoresis was run for 90 min at 120 mV. After 1 h of protein transfer at 100 mV, blots were washed, blocked and incubated overnight using CDH1-, XBP1-, CD44- and GAPDH-specific antibodies. The HRP-bound secondary antibody was added for 1 h under exclusion of light before blots were developed using TF's Pico PLUS chemiluminescence substrate for ECL.

## Results & discussion

### Physico-chemical characterization and stability of HA-coated polyplexes

To non-covalently immobilize anionic molecules as targeting moiety on the surface of PEI Px, core PEI-siRNA nanoparticles bearing a positive zeta potential were produced and subsequently allowed to electrostatically adsorb negatively charged HA ("2-step-coating"; Fig. 1a) similarly to previously described layer-by-layer approaches.[39] A second approach included the initial formation of PEI-HA intermediates, which then interacted with siRNA in the following step ("inverse 2-step-coating"; Fig. 1b). Whereas the Px obtained with this approach may suffer from poorer ligand exposure on the polyplex surface, they can possibly modulate the release of siRNA from the Px better, which is still a major concern in current nucleic acid delivery strategies.[40,41] The incorporation of HA into the core could attenuate PEI-siRNA (electrostatic) interactions, potentially facilitating siRNA release. Alternatively, the coating process can be simplified in a third approach by blending the anionic components (HA and siRNA) and combining them directly with cationic PEI in one single step ("1-step-coating"; Fig. 1c). However, this uncontrolled assembly may also fail to adequately expose the targeting ligand on the polyplex surface, resulting in impaired CD44-HA interaction and polyplex internalization.

To assess differences among the three mentioned coating procedures and to evaluate the successful immobilization of varying amounts of HA on or in the Px while keeping PEI and siRNA amounts constant at a N/P ratio of 5, the particles were examined using DLS and LDA analyses. In summary, all three approaches successfully produced Px of comparably favorable sizes and PDIs. The successive drop in zeta potential ($\zeta$) with increasing amount of HA implies effective coating of the Px (Fig. 1). These results indicate that the physico-chemical characteristics mainly depend on the chosen HA : PEI-ratio (w/w) and not necessarily on the coating procedure, effectively subdividing the nanoparticles into three major groups: with positive, near neutral or negative surface charge.

In the first group, Px and HAPx with 1 : 5 or 1 : 2.5 coating ratios exhibited mean sizes around 110–130 nm, mean PDIs from 0.13 to 0.18 and a strong positive surface charge of 26–36 mV ($HAPx^{+\zeta}$). The second group of HAPx with 1 : 1 and 2.5 : 1 ratios depicted particles transitioning from a positive to negative zeta potential (+19 mV to −18 mV) with increased sizes of 160–300 nm and even above 400 nm (2.5 : 1) for the 1-step-coating ($HAPx^{\pm\zeta}$). Here, the coating approach had a decisive impact on the particle sizes, especially for HAPx 2.5 : 1 with close-to-neutral zeta potential, where the smallest size increase was observed for HAPx obtained by the standard 2-step coating. Similar to these findings, Tirella *et al.* as well as Yamada *et al.* produced bigger-sized HA : polycation complexes at ratios close to the effective compensation between positive and negative charges.[42,43] In group 2, net-charges are balanced to form Px of almost neutral zeta potential. The missing electrostatic repulsion consequently leads to polyplex aggregation. Nevertheless, group 2 HAPx exhibited a desirable, monodisperse particle distribution with PDIs ranging from 0.04 to 0.11. In the third group, strongly negatively charged (−26 to −30 mV) HAPx with 5 : 1 and 10 : 1 ratios formed smaller particles of 120 to 140 nm in size ($HAPx^{-\zeta}$) but exhibited a broader particle size distribution (PDI: 0.10 to 0.18).

The colloidal stability of the formulation was evaluated over time and is shown in ESI Fig. S1,† displaying the course of PX sizes during 6 weeks of storage at room temperature (23 °C). Px, $HAPx^{+\zeta}$ and $HAPx^{-\zeta}$ showed sustained stability with minor deviations in the hydrodynamic diameter. The magnitude of size change was driven by the coating procedure with a minimal mean change in size for the 2-step coating (11%) and a maximal mean change for the 1-step coating (29%). The same tendency was also observed to a greater extent for $HAPx^{\pm\zeta}$ particles. This group of HAPx was the least colloidally stable, especially HAPx 1 : 1, which aggregated within the first 2 to 4 weeks ($d_h$ + 272–618%). As mentioned above, the weaker electrostatic repulsion at near-neutral zeta potential is expected to cause particle aggregation over time.

### HA-coating improves polyplex stability in the presence of polyanionic species at neutral pH

Upon systemic administration, Px face a variety of stressors including opsonization by biomolecules such as proteins, lipids and polysaccharides that determine their stability and clearance from the circulation, and thus ultimately their therapeutic efficacy.[44,45] Particularly, anionic species within the serum can bind to the surface of cationic nanoparticles and competitively displace anionic siRNA molecules from their binding sites within the nanoparticles, compromising the therapeutic efficacy.

Initially, it was investigated whether during the different HA-coating procedures complete siRNA encapsulation was achieved. As mentioned above, anionic HA used during polyplex formulation may negatively influence siRNA encapsulation. The SYBR-gold assays suggest that siRNA was efficiently encapsulated at all HA : PEI ratios regardless of the coating procedure (Fig. 2a). Marginal release (<2%) of siRNA was observed starting from HAPx 2.5 : 1 onwards but remained stable even at higher ratios (20 : 1). Surprisingly, polyplexes produced *via* the Inverse 2-step coating showed superior encapsulation efficiency at high HA-PEI ratios, even though negatively charged HA-PEI core particles may prevent siRNA binding due to repulsion. Overall, it was concluded that the siRNA displacement by HA is insignificant within the reported range of HA : PEI ratios.

Subsequently, the heparin competition assay was applied to test whether HA-coating can improve polyplex stability in the presence of the polyanionic species found in the systemic circulation. According to the Derjaguin–Landau–Verwey–Overbeek (DLVO) theory, a negative zeta potential of HA-coated PEI nanoparticles should prevent interaction with anionic species due to increased repulsion.[46] Fig. 2a–c indicate comparable release profiles for the 3 coating procedures with Px to extensively release siRNA at 0.5 IU heparin, reaching a maximum of 50–60% at 1.0 IU heparin. Interestingly, coating of Px particles with HA significantly reduced siRNA release at high heparin concentrations, with less than 10% release for the 2.5 : 1 HA : PEI ratio. Bigger-sized, near-neutral Px (HAPx 1 : 1 and 2.5 : 1) show an overall reduced siRNA release compared to the other formulations, which can be explained by their ability to incorporate higher amounts of siRNA molecules per particle and thicker shielding layer, decreasing their total accessibility for heparin.

To summarize, all HA-coating procedures enhanced polyplex stability in the presence of polyanions. However, as observed for group 3 HAPx, incorporating an extensive amount of HA may weaken the siRNA binding, which in turn facilitates siRNA release.

### Near-neutral HAPx species incur a smaller protein corona and show improved stability in high protein content environments

The adsorption of proteins on the surface of nanoparticles that occurs during systemic circulation is referred to as protein corona formation.[47] Its dimension and composition heavily depends on the physico-chemical properties of the nanoparticles.[48,49] Thus, alterations of the latter characteristics

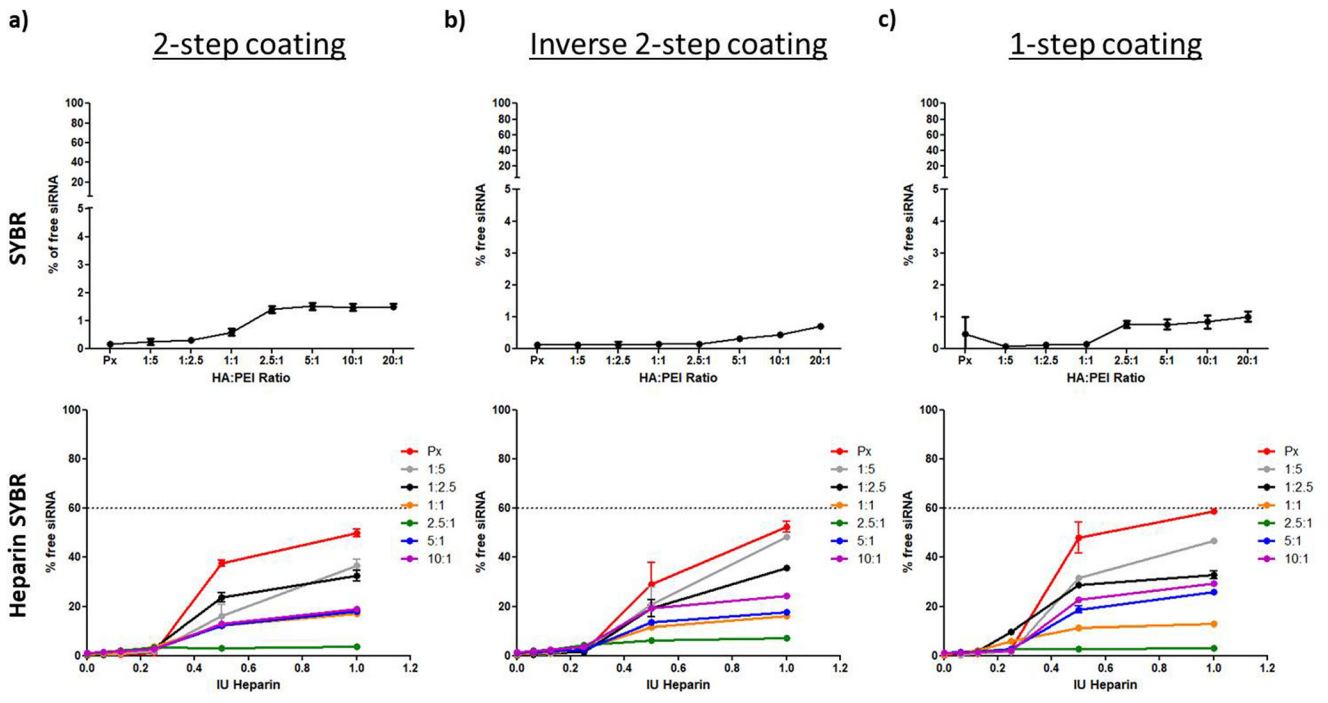


Fig. 2 HA : PEI-ratio (w/w) dependent siRNA encapsulation efficiency (upper panel) and siRNA release profile at pH 7.4 (lower panel) of particles produced *via* (a) 2-step coating, (b) inverse 2-step coating, or (c) 1-step coating assessed by SYBR gold intercalation with siRNA ($n$ = 2). The lower panel demonstrates relative SYBR gold fluorescence intensity with respect to heparin competition (international units [IU]). The black dotted line represents maximal siRNA release of uncoated Px particles at the highest heparin concentration (1 IU).

 

*via* HA-coating of the Px are prone to affect protein-particle interaction and thereby their overall stability. First, this effect was investigated using a simple DLS set-up to visualize changes of size and zeta potential. Therefore, Px and HAPx were incubated in buffer containing 2% FBS (ESI Fig. S2a and b†). At higher FBS concentrations, auto-fluorescence and scattering impede reliable analysis. DLS/LDA results of the particles after incubation were compared to particles incubated in FBS-free buffer. Exposure to 2% FBS led to a charge inversion of all initially positively or neutrally charged particles. The resulting negative zeta potentials ranging from −15 mV (Px) to −25 mV imply intense absorption of proteins on the surface of the nanoparticles (Fig. S2a†). In line with these findings, the size increase of Px after incubation with serum was more pronounced for initially positively charged particles than for $HAPx^{\pm\zeta}$ and $HAPx^{-\zeta}$ (Fig. S2b†). Hence, according to this approximation, HA-coating not only shields siRNA from displacement but also attenuates uncontrolled protein binding.

Second, to investigate polyplex stability under *in vitro*- (10% FBS) or *in vivo*-like conditions (90% FBS), a fluorescence-based assay that relies on de-quenching (FQbA) to approximate polyplex stability was applied. Complexation of fluorescently labeled siRNA leads to quenching of the fluorescence intensity (ESI Fig. S2c†). Upon disassembly or release, the siRNA is expected to de-quench. This de-quenching phenomenon was exploited to indirectly evaluate polyplex stability over time incubated in 10 mM HEPES (buffer), 10% FBS and 90% FBS.

Fluorescence intensity (FI) was reduced to 20–35% of the maximum intensity (relative to free siRNA) in regular buffer and remained relatively constant during the 240 minutes of observation, indicating sustained stability of the Px (Fig. 3a). The distinct coating methods did not considerably affect the course of quenching. Fluctuations in the fluorescence intensity observed in the first 10 min might be explained by the reorganization of Px after being pipetted into the well plate. Likewise nano-formulations were stable in 10% FBS-containing buffer (Fig. 3b). Quenching levels started and persisted at 10–20% of the maximum FI. The drop of the FI-baseline in comparison to the FBS-free buffer can be explained by the reinforced polyplex condensation. It is well documented that elevated external osmotic pressure in 10% FBS-containing buffers leads to particle shrinkage,[52,53] which in turn explains enhanced fluorescence quenching of labeled siRNA molecules.

Upon incubation in 90% FBS, however, Px initiated disassembly as indicated by pronounced de-quenching within the first 120 min (Fig. 3c). $HAPx^{+\zeta}$ and $HAPx^{\pm\zeta}$ Px outperformed uncoated Px and $HAPx^{-\zeta}$. Strikingly, the latter Px (HAPx 5/10 : 1) de-quenched considerably faster and to a higher extent than the standard Px, especially for the "inverse 2-step coating" (100% release after 30 min). PEI-HA core Px with a high HA content may have facilitated release of surface-bound siRNA molecules due to a weakened PEI-siRNA attraction. Indeed, a similar effect was observed by Greco *et al.* in the case of co-incorporation of anionic species into mPEG-b-P

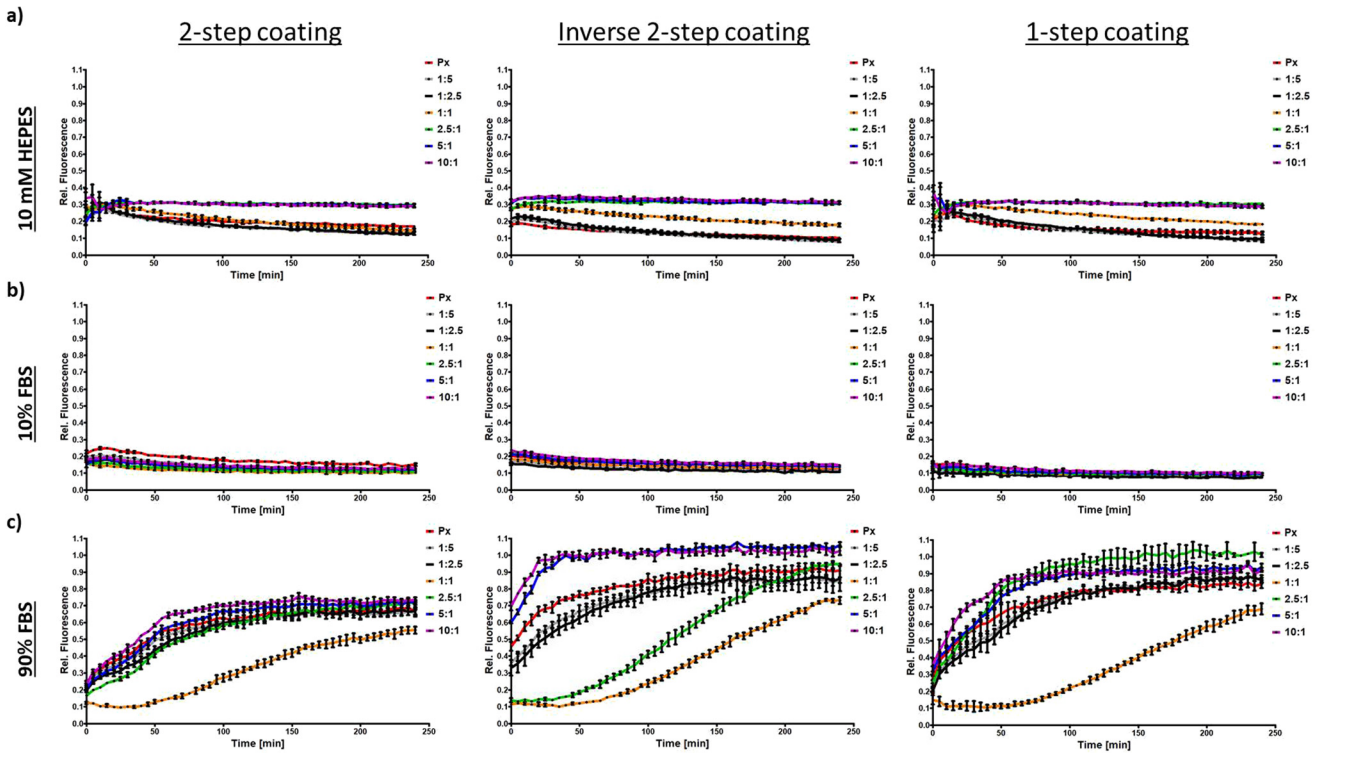


**Fig. 3** HA : PEI-ratio dependent stability of HAPx in 10 mM HEPES pH 7.4 (a), 10% FBS (b), and 90% FBS (c) prepared by 2-step coating (*left*), inverse 2-step coating (*middle*) and 1-step coating method (*right*) (data points indicate mean ± SD, $n$ = 3). Release or decompaction of AF647-labeled siRNA is indicated by an increase in the relative fluorescence intensity normalized by free siRNA (shown in %).

(APNBMA) Px. They demonstrated facilitated release of siRNA once PAA, bearing a high anionic charge density, was co-encapsulated, which they related to altered nucleic acid binding properties.[41]

Remarkably, HAPx 2.5 : 1 (green line) and in particular HAPx 1 : 1 (orange line) displayed an overall superior stability. In the case of HAPx 2.5 : 1, the particles meet the de-quenching levels of standard Px after about 100 min (2-step) and 190 min (inverse 2-step) of serum incubation. HAPx 1 : 1 particles, regardless of the coating procedure, remained intact over the first 100 min and then slowly disassembled, still maintaining 35–45% quenching at the end of the observation time period. Earlier studies indicated that bigger particle sizes (smaller surface area per volume) and near-neutral surface charges of nanocarriers reduce protein–particle interaction, resulting in improved colloidal stability.[50–52] Regardless of the HA : PEI ratio, particles produced *via* 2-step coating exhibited higher stability compared to the other formulations, as indicated by less de-quenching observed throughout the measurement and especially at the final time point of 240 min.

### Fluorescence correlation spectroscopy (FCS) was used to assess stability of the 2-step coated HAPx 2.5 : 1 HA : PEI ratio group in high protein content environments

The FQbA assay represents a simple and rapid method to indirectly assess the (in)stability of polyplexes over time. As it can be performed in a plate-reader, it can be used to simultaneously probe many samples, in a high-throughput manner. However, multiple factors may contribute to de-quenching, such as complete polyplex disassembly, with the corresponding siRNA release, or nanoparticle swelling, which increases spatial fluorophore separation and reduces quenching.

Therefore, FCS was used to evaluate the stability of 2-step coated HAPx in high protein content environments in more detail. FCS is a highly sensitive (picomolar to nanomolar regime) technique that evaluates the intensity fluctuations caused by the diffusion of a fluorescently labeled molecule through the small observation volume of a confocal microscope. Time-dependent fluctuations of the fluorescence signals are analyzed using an autocorrelation analysis, which provides information about sample concentration, brightness and mobility (translational diffusion coefficient).[37] Previously, Nuhn *et al.*[53] used the autocorrelation function (ACF) to discriminate between intact Px and free siRNA molecules, thanks to their great difference in size and thus diffusion coefficient. Indeed, a slow diffusion, due to large molecular size or high medium viscosity, will shift the ACF decay towards longer time scales.

More recently, the Nuhn lab also showed that FCS can be used to evaluate nanoparticle integrity in a complex yet therapeutically relevant protein-rich context such as blood plasma.[54] Overall, the principle of FCS allows to assess polyplex stability in different buffer environments with higher selectivity compared to the FQbA assay. FCS can discriminate between polyplex disassembly and swelling: intact but restructured polyplexes still exhibit slow diffusion, whereas complete disassembly results in the presence of freely diffusing siRNA, with a correspondingly faster diffusion coefficient.

In a standard confocal setup such as the one used here, only one sample at the time can be evaluated with FCS, making it a low-throughput approach compared to FQbA. Thus, we limited the FCS analysis to only one HA : PEI ratio.

Px and HAPx 2.5 : 1 prepared with 2-step coating were measured *via* FCS in HEPES as a control, and 10% and 90% FBS to mimic *in vitro* and in *in vivo* like conditions. This HAPx formulation was found to be the most promising candidate since it showed superior stability in the high protein content environment (Fig. 3c) as well as against heparin compared with uncoated Px (Fig. 2).

Fig. 4a displays well-separated ACF profiles of free siRNA, Px and HAPx in HEPES buffer measured right after particle preparation and after 120 min of incubation. In accordance with the above findings, neither of the formulations showed alterations in their diffusion profile, implying sustained stability. The bigger size of HAPx, and thus slower diffusion (ESI Tables S1 and S2†), is reflected in the shift of the respective ACF curves to slower time scales. Likewise, investigations on stability in 10% FBS-containing buffer confirmed persistent polyplex integrity for both formulations (Fig. 4b and ESI Table S2†). As we expected fast disassembly kinetics in 90% FBS, we acquired intermediate time points at 30, 60 and 90 min respectively. Strikingly, as shown in Fig. 4c, the ACF of uncoated Px instantly approached the ACF of free siRNA at $t_0$, indicating the fast and nearly complete polyplex disassembly upon administration, as described before.[55] At later incubation times, the ACFs of Px and siRNA remain superposed, and the extracted diffusion coefficients were similar to that of si-RNA, emphasizing complete particle rupture and siRNA release (ESI Table S3†). In contrast, the ACF profile of HAPx at $t_0$ mostly resembled the one in HEPES/10% FBS (Fig. 4d). The curve begins to decay at earlier time points, being indicative for the appearance of a second, fast-diffusing component *i.e.* free/decomplexed siRNA (ESI Table S3†). At $t_{30}$, this fast-decaying component phenomenon is increasingly pronounced as the ACFs of HAPx and free siRNA further converged. Hence, the portion of intact particles decreased over time concomitantly with siRNA release from the complex. The data further suggests that, after 60 and 90 min, the majority of Px dissembled. However, a small percentage of HAPx seemed to persist. As demonstrated in ESI Fig. S3a–f,† this tendency was reproducible among other biological replicates underlining the advantageous stability profile of HAPx particles.

Overall, these data correlate the de-quenching observed in Fig. 3c with polyplex disassembly and siRNA release rather than a conformational change within the particles. In accordance with FQbA, FCS measurements confirmed the superior stability of HA-coated Px ($HAPx^{+\zeta}$) over uncoated Px. However, considering the single molecule selectivity and higher sensitivity of FCS, it appeared that disassembly kinetics under *in vivo*-like conditions were underestimated by the de-quenching assay. Px disrupted immediately after administration in

 

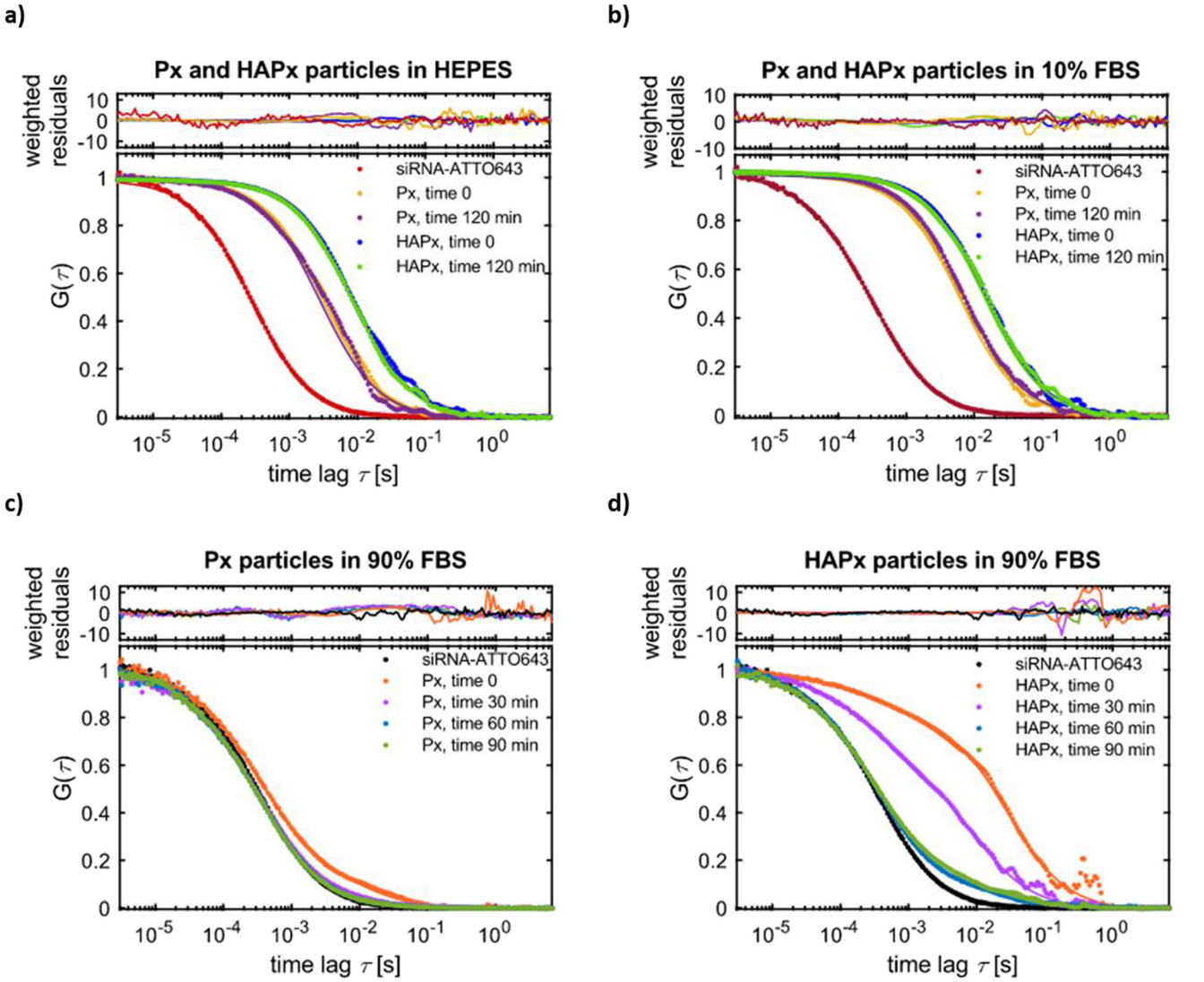


**Fig. 4** FCS analysis of Px particles and coated HAPx particles. The particles were prepared with 15% ATTO643-labeled negative control siRNA and 85% unlabeled 25/27mer siRNA directed *versus* eGFP. HAPx particles were formulated at an HA : PEI ratio of 2.5 : 1 with 2-step coating. (a) Representative autocorrelation functions (ACFs) of Px particles and coated HAPx particles in 10 mM HEPES buffer immediately after dilution and 2 h later. (b) Representative ACFs of Px particles and coated HAPx particles in 10% FBS immediately after dilution and 2 h later. (c) Representative ACFs of uncoated Px particles at different time points of incubation in 90% FBS. Note that the ACFs relative to the time points from 30 to 90 min largely overlap with the siRNA-ATTO643 curve. (d) Representative ACFs of coated HAPx particles at different time points of incubation in 90% FBS.

high protein content buffer whereas HAPx remained stable for at least 30–60 min, which can be partially attributed to differences in their surface properties.

As the majority of proteins adsorbed on nanomaterials possess an isoelectric point <7.4, positively charged nanocarriers are particularly vulnerable to adsorption events *in vivo*.[8] Indeed, it was reported that polyplexes made from branched, high molecular weight PEI induced aggregation of blood cells, conformational changes of proteins and impaired blood coagulation.[56] These toxic effects were mainly attributed to their physico-chemical properties, in particular to the highly positive surface charge and the resulting interaction potential of the drug delivery system. Likewise, strongly positively charged nanoparticles are prone to rapid systemic clearance since they preferentially interact with negatively charged proteoglycans present at the glomerular basal membrane or are internalized by macrophages of the reticuloendothelial system (RES) after opsonization.[8,56,57] The present study demonstrates how HA-coating of cationic Px allows fine-tuning of their physico-chemical characteristics, decreasing biomacromolecule-particle interaction (ESI Fig. S2†), and thereby potentially enhancing their stability (Fig. 3 and 4) and ultimately the performance of the drug delivery system *in vivo*. A near-neutral zeta potential increased stability against competing polyanions (Fig. 2b). As was postulated by Zheng *et al.*, this will inevitably result in decreased interactions with macrophages and conse-

quently prolong the half-life of the nanocarriers during systemic circulation.[58] Likewise, the modified surface chemistry of HA-coated particles decisively influences the protein corona formation and affects colloidal stability in high protein environments. With our results, we support previous theories on stealth- and electrostatic shielding properties of HA-bearing nanosystems employing DLS and fluorescence-based approaches.[29,59–62]

### *In vitro* evaluation of HAPx in a cell line based EMT-model

**Highly selective uptake and increased endocytosis of HAPx$^{\pm\zeta}$ in CD44-overexpressing EMT-positive BC cell lines.** Besides enhancing nanoparticle stability, HA-coatings provide nanoparticles with a targeting moiety for selective endocytosis *via* the HA-binding protein CD44 or RHAMM, both overexpressed in cancer tissues.[29,59,63,64] As CD44 overexpression has been correlated with EMT in breast cancer, the capability of HAPx to specifically target EMT undergoing or undergone cells *via* CD44-mediated uptake was evaluated in different established EMT-model breast cancer cell lines.[22] The uptake study investigated several factors that contribute to intracellular delivery, namely receptor status and isotype expression, the impact of physico-chemical parameters and HA coating of the Px on uptake, as well as intracellular fate. These aspects are discussed in the following paragraphs.

Flow cytometry was employed to confirm that CD44 expression increases with higher EMT status (MCF7 < HCC1954 < MDA-MB-468 < MDA-MB-231) (Fig. S4a†). Cell lines were categorized as CD44$^{low}$ (MCF7), CD44$^{medium–low}$ (HCC1954), CD44$^{medium–high}$ (MDA-MB-468) and CD44$^{high}$ (MDA-MB-231). RHAMM-mediated uptake was ruled out due to negligible RHAMM surface expression in all cell lines. These findings emphasize CD44's potential in HA-based cancer therapies (Fig. S4b†).

Additionally, expression of CD44 isoforms in the four cell lines was assessed with western blotting using a pan-CD44 antibody, which allows the detection of all CD44 species, by binding a conserved region of the protein across splicing variants (Fig. S4c†). The patterns varied significantly across cell lines with the epithelial cell line MCF7 (high levels of CDH1) showing no significant CD44s or CD44v bands. MDA-MB-231 mesenchymal-like cells (absence of CDH1) exhibited high CD44s, while HCC1954 and MDA-MB-468 showed elevated CD44v levels (MB-468 > HCC1954). Notably, these findings were congruent with recent studies that highlight CD44-isoform expression heterogeneities among differently graded breast cancer.[26,65]

To verify HA-mediated endocytosis of the different HAPx species produced *via* 2-step coating, particle uptake was assessed 24 h after transfection (Fig. 5). To approximate the impact physico-chemical characteristics of HAPx species exert on cellular uptake, the hydrodynamic diameter $d_h$ (green line) and zeta potential $\zeta$ (orange line) of polyplexes in 10 mM HEPES were superimposed with the relative uptake to Px (dotted lines) in the various cell lines. Ideally, physico-chemical parameters should be assessed in 10% FBS; however, the acquisition of such data (*e.g.*, zeta potential) is limited due to the complexity of the culture medium and the presence of proteins, particularly globulins. According to CD44 cell surface expression levels, the highest uptake was expected to occur in MDA-MB-231 cells with HAPx in comparison to Px. However, polyplex internalization was found to be more complex with efficacy depending on CD44 isotype, HAPx species and coating procedure.

Notably, uptake of HAPx in CD44$^{null}$ (grey dotted line) and CD44v$^{low}$ (light blue dotted line) cell lines decreased considerably with increasing HA : PEI-ratio as compared to uncoated Px (CD44$^{null}$ < CD44v$^{low}$) passing a minimum for the HAPx$^{\pm\zeta}$ species. The latter formulations were internalized up to 68% less (CD44$^{null}$, Fig. 5a) whereas HAPx$^{-\zeta}$ Px internalization again approached uptake levels of Px. These findings can be partially explained referring to the physico-chemical characteristics of the different polyplex groups. Smaller, highly positively charged (HA)Px$^{+\zeta}$ exhibited the strongest interaction potential with the negatively charged surface of the cell membrane. HAPx$^{-\zeta}$ displayed similar (small) sizes but had decreased cellular interaction due to their negative zeta potential. Both, the bigger sizes and decreased/negative surface charges of HAPx$^{\pm\zeta}$ were detrimental for endocytosis of nanoparticles accounting for the lowest uptake. In total, the course of uptake was indirectly proportional to the hydrodynamic diameter of Px. It further appeared that CD44 expression still contributed to the 20% increase in overall mean uptake of HAPx in CD44v$^{low}$ over CD44$^{null}$ cells.

Strikingly, the course of internalization showed a different picture for CD44v$^{high}$ (dark blue dotted line) and CD44s$^{high}$ (purple dotted line) cell lines, confirming a clear relationship between HA : PEI-ratio and maximum uptake for the HAPx$^{\pm\zeta}$ species (140% of Px, Fig. 5a). Here, relative nanoparticle internalization was directly proportional to the hydrodynamic diameter of Px, whereas the contribution of the zeta potential was insignificant.

Finally, comparison of cellular uptake with the other two coating procedures (ESI Fig. S5†) revealed strong similarities with particles produced with the inverted-coating procedure. In contrast, 1-step coated Px followed a different internalization tendency with elevated uptake for HAPx$^{-\zeta}$ implying distinct HA-surface presentation among the coating procedures. Although, according to the physico-chemical evaluation of HAPx, coating procedures had moderate influence on particle properties and stability, *in vitro* uptake showed clear differences. This indicates that HA-molecules are differently exposed on the particle surface based on the coating method. This is in agreement with previous findings reporting that polyplex morphology and intra-particulate arrangements of HA-coated nanoparticles decisively impact HA-presentation and thereby tune the affinity towards its receptor CD44.[62,66]

Uptake *via* receptor-mediated endocytosis will eventually guide nanoparticles towards *endo*/lysosomal compartments. To study their intracellular fate and to compare and quantify the different courses of internalization between CD44$^{null}$ and CD44v$^{high}$ cell lines (Fig. 5a), confocal imaging was combined

 

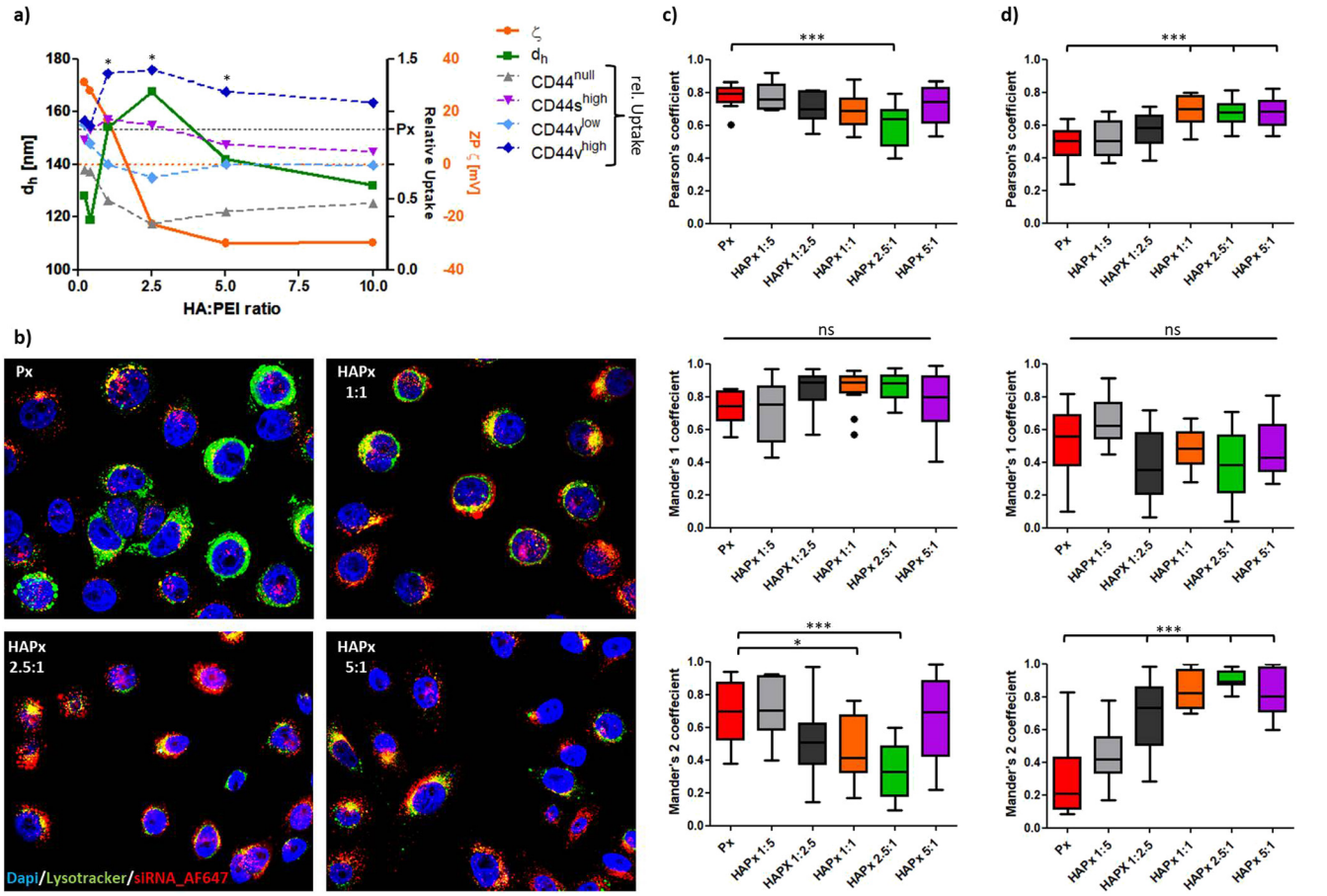


**Fig. 5** (a) CD44 (isotype, expression level) and HA : PEI-ratio dependent cellular uptake of HAPx particles produced *via* 2-step coating measured by flow cytometry. The mean relative uptake normalized to Px (black-dotted line, right *y*-axis, $y = 1$) is shown as a dotted line with the grey ($CD44^{null}$ MCF7), purple ($CD44s^{high}$ MB-231), light blue ($CD44v^{low}$ HCC1954) and dark blue ($CD44v^{high}$ MB-468) color indicating the cell line/CD44-isotype expression level. Solid lines represent the mean physico-chemical properties of respective HAPx species with respect to hydrodynamic size (green) and zeta potential (orange) shown on the left and right *y*-axis, respectively. Orange dotted line ($y_{right,\ orange}$) depicts zeta potential at 0 mV. (b) Confocal images of MDA-MB-468 cells transfected with different 2-step coated HAPx Px containing AF647-labeled siRNA (red) for 24 h. Cells were stained for the nuclei (DAPI, blue) and *endo*/lysosomal compartments (Lysotracker®, green). The yellow color indicates intracellular co-localization of particles with lysosomes. (c and d) JACoP co-localization analysis ($n$(cells) ≥ 12) of AF647-labeled siRNA (red) and lysotracker (green) in MCF7 (c) and MDA-MB-468 (d) cell lines transfected HAPx for 24 h. Pearson's correlation coefficient (upper panel) and Manders' correlation coefficients 1 (central panel, "red-in-green") and 2 (lower panel, "green-in-red") are shown as whiskers plot. Asterisks above the lines and bars indicate level of significance. (*$p$-value < 0.05; ***$p$-value < 0.001). Error bars in c and d indicate standard deviation SD.

with "JACoP" (ImageJ) co-localization analysis (Fig. 5b–d). The Pearson's correlation coefficient (PCC) was used to assess the linear relationship between the signal intensities of two fluorophores, where a value of 1 corresponds to complete positive correlation and a value of 0 indicates no correlation. However, the significance of the PCC for co-localization events is disputable as values are highly sensitive to differences in signal intensities of the respective channels and to background noises, hence to thresholding. Instead, the Manders' correlation coefficients ($M_1$ and $M_2$) were therefore used to quantify the extent of spatial co-occurrence of the two fluorophores, *i.e.* labeled Px and labeled *endo*/lysosomes, with values of 1 reflecting 100% co-localization.[67,68] Here, the $M_1$ coefficient relates to the proportion of polyplexes that are trapped in lysosomes, whereas the $M_2$ coefficient indicates the proportion of lysosomes containing polyplexes. Notably, Pearson's and Manders' coefficient synergize as the latter quantifies signal co-occurrence and the former quantifies the degree of correlation within the co-occurring signal.

Confocal images showed elevated accumulation of 2-step coated HAPx 1 : 1, 2.5 : 1 and 5 : 1 within lysosomes of $CD44v^{high}$ MDA-MB-468 cells indicated by pronounced co-localization (orange) of labeled siRNA (red) with the LysoTracker™ (green) stain after 24 h of incubation (Fig. 5b). HA-coated Px showed juxtanuclear positioning indicative of successful receptor-mediated endocytosis, which was less frequently observed in the case of Px particles. According to the JACoP image analysis shown in Fig. 5c, strong association of uncoated Px was observed with lysosomes of CD44null MCF7 cells as indicated by a median PCC of 0.80. The PCC decreased

for HA-coated species, which was significant in the case of HAPx 2.5 : 1 ($P < 0.001$). Simultaneously, the fraction of *endo*/lysosomes bearing HAPx$^{\pm\zeta}$ species (M2) was significantly reduced to less than 50%. Still, most internalized particles accumulated within lysosomes independent of HA : PEI-ratio ($0.75 < M1 < 0.90$). Instead, endocytosis of uncoated Px in CD44vhigh MDA-MB-468 cells revealed the lowest correlation with lysosomes (Fig. 5d, *M*2). Notably, the PCC of HAPx 1 : 1, 2.5 : 1 and 5 : 1 was significantly elevated ($P < 0.001$) which is in good agreement with data obtained from flow cytometry (Fig. 5a). Likewise, the proportion of lysosomes comprising HAPx 1 : 2.5 and the latter three polyplex types was significantly increased compared to uncoated Px. Specifically, 70–90% of lysosomes co-localized with HAPx opposed to only 28.5% (mean M2-value) for Px. However, the fraction of polyplexes reaching lysosomes ($M_1$) was insignificantly distinct among the nano-formulations but on average less than observed in CD44null MCF7 cells.

In summary HA-functionalization of polyplexes entailed overall increased association (PCC) of particles with lysosomes in CD44v-expressing cells but decreased association in CD44 deficient MCF7 cells, implying a high degree of uptake-selectivity. Presumably, the contribution of HA/CD44-mediated endocytosis enabled HAPx species to accumulate in a higher fraction of lysosomes compared with overall lower uptake in the CD44$^{null}$ cell line, possibly due to the unfavorable physicochemical characteristics of HA-coated polyplexes as well as lacking CD44 expression ($M_2$). The data further suggest that all polyplexes were preferentially taken up *via* active endocytosis mechanisms referring to the high fraction of particles co-occurring in lysosomes ($M_1$), regardless of coating. The substantially lower fraction of $M_1$ in MDA-MB-468 than in MCF7 cells may be indicative for enhanced endosomal escape but may also relate to differences of the endocytic machinery between cell lines.

**CD44-R isoforms follow different uptake kinetics.** The relationship between EMT-status and CD44-expression is further complicated by the existence of distinct isoforms as well as by the phenomenon of isotype switching, altering the CD44v/s-expression ratio as was shown for growth factor-mediated EMT induction in MDA-MB-468 (ESI Fig. S6a and b†).

To better distinguish between CD44v- and CD44s-mediated uptake, earlier time points (1 h and 4 h) after transfection with Px and HAPx (1 : 2.5, 1 : 1 and 2.5 : 1) in CD44v$^{high}$/CD44s$^{low}$ MDA-MB-468 and CD44v$^{low}$/CD44s$^{high}$ MDA-MB-231 cells were investigated. The CD44v$^{low}$/CD44s$^{low}$ MCF7 cell line (CD44$^{null}$) was included as a negative control. The data revealed increased uptake (167%) of HAPx 1 : 1 in CD44s$^{high}$ cells already 1 h after transfection. On the contrary, uptake of the same HAPx species was dramatically reduced in CD44$^{null}$ (5% of Px) and CD44v$^{high}$ (23% of Px) cell lines (Fig. 5e). Internalization of HAPx 1 : 1 stagnated in CD44s$^{high}$ cells (137% of Px after 4 h) but considerably increased to over 345% in CD44v$^{high}$ cells after 4 h (Fig. 5e). At the same time, transfection with both HAPx$^{\pm\zeta}$ species remained below 20% of Px in CD44$^{null}$ cells, underlining the correlation of CD44 (s/v) receptor expression and HAPx uptake. HAPx 1 : 2.5, physico-chemically resembling Px particles, showed a low but overall comparable uptake profile to uncoated Px in CD44$^{null}$ cells.

Ultimately, this uptake study implies that the conceptual idea of specifically targeting EMT *i.e.*, a more mesenchymal phenotype *via* HA-CD44-R interactions is realizable by means of HA-coatings of the Px. Referring to Fig. 5a and e, HAPx$^{\pm\zeta}$ Px displayed a highly selective uptake for the EMT-positive cell lines MDA-MB-468 and MDA-MB-231. Selectivity was confirmed by decreased uptake (compared to uncoated Px) in epithelial MCF7 (−68.0%) and HCC1954 cells (−34.5%) but a concomitant increase in mesenchymal cells (2.6- to 5.6-fold). Likewise, HA-coated octa-arginine gene vectors efficiently induced transgene expression in CD44$^{high}$ HCT116 cancer cells, which was instead significantly compromised in CD44$^{low}$ NIH3T3 cells.[43] Since MCF7 cells exhibit features of differentiated mammary epithelium,[69] the data suggest that HA-coated nano-formulations preferably interact with CD44$^{high}$ malignant cancer cells, sparing the healthy epithelium cells. It is thought that ligand distribution on the nanoparticle surfaces governs the efficacy of receptor-mediated endocytosis with a uniform ligand distribution leading to optimal uptake.[70] Indeed, the precise formulation development of HA-coated nanoparticles was found to be key for the desired targeting concept. The HA : PEI-ratio, coating strategy and the resulting physicochemical differences heavily impacted its success.

Second, our data indicate that CD44s-R uptake kinetics are faster in the early phase but probably suffer from receptor saturation at later time points compared to CD44v-R (Fig. 5a and e). After 1 h, CD44s$^{high}$ MDA-MB-231 cells incorporated HAPx 1 : 1 particles twice as fast as CD44v$^{high}$ MDA-MB-468 cells and about 6-times faster than CD44$^{null}$ MCF7 cells. However, after 24 h, this beneficial effect was no longer observed, and uptake values were similar to that of Px. These findings are consistent with a study by Spadea *et al.*, who investigated uptake of fluorescently-labeled HA in the same cell lines.[65] They observed efficient HA uptake in MDA-MB-231 cells with a high score for HA binding after 1 h and a moderate score for internalization after 24 h. In contrast, CD44v expressing MDA-MB-468 cells were attributed a low HA binding capacity due to a faint uptake after 1 h and maintained poor levels of internalization after 24 h. This partially corroborates our data, confirming minimal uptake after 1 h (Fig. 5e) but is in contrast with the observed superior HAPx uptake in this cell line after 4 h and 24 h. MFI values of HAPx 1 : 1 in CD44v$^{high}$ cells increased 10-fold between the 1 h and 4 h time point and remained elevated (1.42-fold normalized to Px) after 24 h. Instead, cells transfected with uncoated Px only exhibited a 3-fold increase in the same timeframe (1–4 h). Thus, here we conclude a slower but increased net uptake of HAPx *via* the CD44v-R isoform(s) as compared to CD44s-R. Possible cell line peculiarities regarding endocytic processing[71] and the fact that HA-decorated particles were used rather than free HA leaves room for additional interpretation. Notably, the glycosylation state of CD44, which is cell line dependent, inversely correlates

 

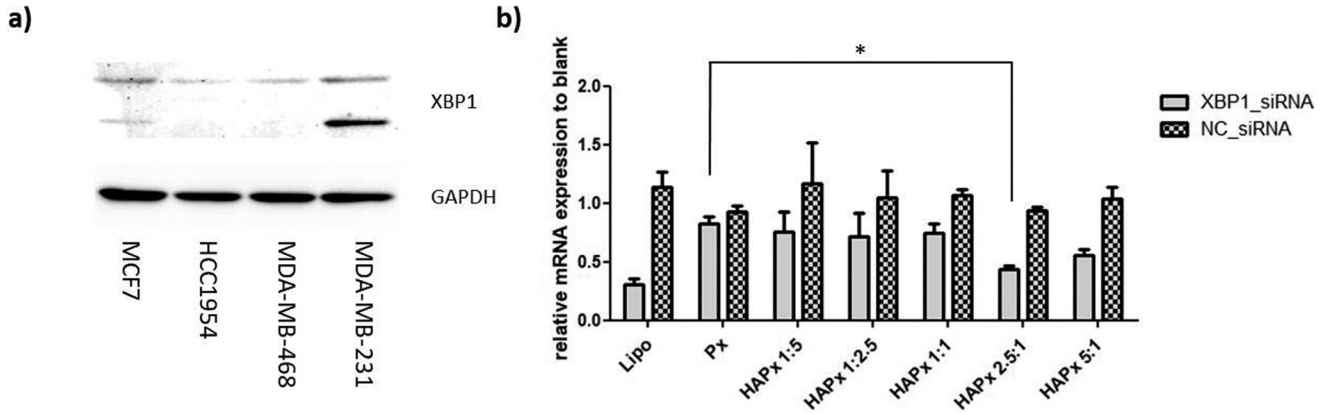


**Fig. 6** (a) Protein levels of XBP1 in the four breast cancer cell lines assessed from a nuclear protein extract. (b) XBP1 mRNA knockdown in MDA-MB-231 cells analyzed *via* RT-qPCR. Results are shown as ΔΔCt-values with error bars indicating the standard deviation SD ($n$ = 2). Consequently and consistent with data from the uptake study, the knockdown efficiency was improved *via* HA-coating when the HA : PEI-ratio was optimized.

with its HA-binding capacity.[11] Furthermore, as stated elsewhere,[66,70,72] the degree of receptor clustering, which depends on particle dimension, ligand exposure and differences in receptor densities (ESI S4a and c†) affects the total number of uptake events, further complicating the scenario. In line with the mentioned literature, the bigger-sized HAPx$^{\pm\zeta}$ species showed the highest uptake explained by their physical size and faster sedimentation in cell culture, allowing for extended cross-linking of CD44 receptors once engaging with the cellular membrane. A strong positive zeta potential seemed to generally relate to higher particle internalization as compared to the negatively charged HAPx species. Moreover, uptake strategies *via* the CD44s-R supposedly suffer from receptor saturation, which was found to be a result of the slow CD44-R turnover and re-presentation at the cell surface after HA binding.[66,73,74] Interestingly, studies indicated that the CD44v isoform has a faster turnaround time,[11] attenuating the receptor saturation effect as was observed in CD44v$^{high}$ MDA-MB-468 cells (Fig. 5a and e). As was postulated by de la Rosa *et al.*, it is also plausible, that the increased size of the isoform variants (CD44v) facilitates receptor-mediated endocytosis as the HA-binding domain is exposed at a greater distance from the cell surface.

**Optimal candidate HAPx 2.5 : 1 showed superior silencing of the XBP1 transcription factor in MDA-MB-231 cells.** Finally, the gene silencing efficiency (at 48 h) of the HAPx species (2-step coating) compared to uncoated Px was examined. A possible molecular target regarding EMT is the transcription factor XBP1 (X-box binding protein 1). Recently, its relevance for EMT was proposed in several publications[33,75–77] and our group demonstrated that EMT induction upregulates XBP1 in breast cancer cells.[22,78] Indeed, high XBP1 protein levels were found in mesenchymal MDA-MB-231 cells compared to the other three cell lines (Fig. 6a).

Transfection of MDA-MB-231 cells (CD44s$^{high}$) with XBP1_siRNA containing lipoplexes (Lipofectamine™ 2000) resulted in a considerable downregulation of XBP1 mRNA (70%), confirming the effectiveness of RNAi (Fig. 6b). Notably, transfection with Px was insufficient to decisively decrease mRNA expression. Introduction of HA *via* the 2-step coating slightly improved knockdown efficiency for HAPx 1 : 5, 1 : 2.5, 1 : 1 and 5 : 1, but the only polyplex formulation mediating significant gene silencing ($P < 0.05$, 55%) was HAPx 2.5 : 1.

Presumably, the enhanced knockdown efficiency was not primarily due to increased particle uptake within the first 24 h. Several effects may synergize such as increased particle internalization due to receptor-mediated endocytosis, decreased protein corona formation, facilitated release of siRNA due to HA and siRNA competing for association with PEI and increased osmotic pressure within HAPx-containing lysosomes relative to vesicles comprising uncoated Px. In further studies, the release kinetics of HAPx need to be investigated. Moreover, a comparison of the knockdown efficiency as a function of CD44 isotype expression would definitely contribute to an overall better understanding of HA-mediated drug delivery.

## Conclusions

Nanoparticulate drug delivery systems comprising HA surface modifications provide carriers with targeting- and stealth-features, which are required to achieve tumor-specific accumulation, reduce off-target effects, and to increase the half-life and stability upon systemic administration. They are also clinically promising candidates in the context of the treatment of cancers undergoing EMT. Notably, more complex, HA-functionalized polymeric nanocarriers were shown to fit into the "3S-transition" concept hypothesized for efficient drug delivery to cancer cells.[29,60] Accordingly, HA-functionalization fulfills stability, surface and size transition requirements as it helps the carrier to protect the drug cargo during circulation for selective interaction with and release in tumor cells *via* CD44-mediated endocytosis. Ultimately, enzymatic size reduction of the HA-functionalized nanoparticles by hyaluronidases at the

tumor site are thought to enable deeper tissue-penetration and hence improve therapeutic efficacy.

Indeed, this study shows the versatile character of HA-coated Px regarding *in vitro* stability and biological performance. Whereas physico-chemical characteristics of differently coated polyplex formulations were shown to be mostly comparable, the coating procedure was identified as a crucial factor during cellular uptake experiments. Ultimately, the ease of the coating methodology and the resultant benefits for particle stability, cell uptake and cancer cell-specificity are upholding the value of HA-coated nanocarriers for drug delivery. HA-coatings provide a therapeutic option for the treatment of otherwise undruggable aggressive types of breast cancer such as those that undergo EMT. The ambiguous nature of CD44 isoforms in receptor-mediated endocytosis, however, may require CD44-expression profiling of patient tumor samples to predict the success of HA-based drug delivery in anticancer therapy and needs to be considered in *in vitro* experiments as well.

## Author contributions

Lorenz Isert: conceptualization, data curation, formal analysis, investigation, methodology, visualization, writing – original draft. Irene Gialdini: data curation, formal analysis, investigation, methodology, methodology, writing – original draft. Thi My Hanh Ngo: data curation, formal analysis. Gabriele Loiudice: data curation, formal analysis. Don C. Lamb: funding acquisition, resources, software, supervision, writing – review & editing. Olivia M. Merkel: conceptualization, funding acquisition, project administration, resources, supervision, writing – review & editing.

## Data availability

All data generated or analysed during this study are included in the main manuscript and in the ESI.†

## Conflicts of interest

The authors have no conflicts to declare.

## Acknowledgements

This work was, in part, funded by the OneMunich Initiative "Munich Multiscale Biofabrication Network", supported by the Federal Ministry of Education and Research.

## References

1 Y. Min, J. M. Caster, M. J. Eblan and A. Z. Wang, Clinical Translation of Nanomedicine, *Chem. Rev.*, 2015, **115**(19), 11147–11190.
2 V. Sanna and M. Sechi, Therapeutic Potential of Targeted Nanoparticles and Perspective on Nanotherapies, *ACS Med. Chem. Lett.*, 2020, **11**(6), 1069–1073.
3 M. Srinivasarao, C. V. Galliford and P. S. Low, Principles in the design of ligand-targeted cancer therapeutics and imaging agents, *Nat. Rev. Drug Discovery*, 2015, **14**(3), 203–219.
4 C. M. Paulos, J. A. Reddy, C. P. Leamon, M. J. Turk and P. S. Low, Ligand binding and kinetics of folate receptor recycling in vivo: impact on receptor-mediated drug delivery, *Mol. Pharmacol.*, 2004, **66**(6), 1406–1414.
5 G. Onzi, S. S. Guterres, A. R. Pohlmann and L. A. Frank, Active Targeting of Nanocarriers, in *The ADME Encyclopedia: A Comprehensive Guide on Biopharmacy and Pharmacokinetics*, Springer International Publishing, Cham, 2021, pp. 1–13.
6 K. Ulbrich, K. Holá, V. Šubr, A. Bakandritsos, J. Tuček and R. Zbořil, Targeted Drug Delivery with Polymers and Magnetic Nanoparticles: Covalent and Noncovalent Approaches, Release Control, and Clinical Studies, *Chem. Rev.*, 2016, **116**(9), 5338–5431.
7 A. C. Marques, P. J. Costa, S. Velho and M. H. Amaral, Functionalizing nanoparticles with cancer-targeting antibodies: A comparison of strategies, *J. Controlled Release*, 2020, **320**, 180–200.
8 C. D. Walkey and W. C. W. Chan, Understanding and controlling the interaction of nanomaterials with proteins in a physiological environment, *Chem. Soc. Rev.*, 2012, **41(7)**, 2780–2799.
9 V. M. Platt and F. C. Szoka Jr, Anticancer Therapeutics: Targeting Macromolecules and Nanocarriers to Hyaluronan or CD44, a Hyaluronan Receptor, *Mol. Pharm.*, 2008, **5**(4), 474–486.
10 J. M. Rios de la Rosa, P. Pingrajai, M. Pelliccia, A. Spadea, E. Lallana, A. Gennari, I. J. Stratford, W. Rocchia, A. Tirella and N. Tirelli, Binding and Internalization in Receptor-Targeted Carriers: The Complex Role of CD44 in the Uptake of Hyaluronic Acid-Based Nanoparticles (siRNA Delivery), *Adv. Healthcare Mater.*, 2019, **8**(24), 1901182.
11 J. M. Rios de la Rosa, A. Tirella and N. Tirelli, Receptor-Targeted Drug Delivery and the (Many) Problems We Know of: The Case of CD44 and Hyaluronic Acid, *Adv. Biosyst.*, 2018, **2**(6), 1800049.
12 J. M. Wickens, H. O. Alsaab, P. Kesharwani, K. Bhise, M. Amin, R. K. Tekade, U. Gupta and A. K. Iyer, Recent advances in hyaluronic acid-decorated nanocarriers for targeted cancer therapy, *Drug Discovery Today*, 2017, **22**(4), 665–680.
13 W.-Y. Huang, J.-N. Lin, J.-T. Hsieh, S.-C. Chou, C.-H. Lai, E.-J. Yun, U. G. Lo, R.-C. Pong, J.-H. Lin and Y.-H. Lin, Nanoparticle Targeting CD44-Positive Cancer Cells for Site-Specific Drug Delivery in Prostate Cancer Therapy, *ACS Appl. Mater. Interfaces*, 2016, **8**(45), 30722–30734.
14 S. Misra, P. Heldin, V. C. Hascall, N. K. Karamanos, S. S. Skandalis, R. R. Markwald and S. Ghatak, Hyaluronan-CD44 interactions as potential targets for cancer therapy, *FEBS J.*, 2011, **278**(9), 1429–1443.

 

15 H. Xu, M. Niu, X. Yuan, K. Wu and A. Liu, CD44 as a tumor biomarker and therapeutic target, *Exp. Hematol. Oncol.*, 2020, **9**(1), 36.
16 C. Chen, S. Zhao, A. Karnad and J. W. Freeman, The biology and role of CD44 in cancer progression: therapeutic implications, *J. Hematol. Oncol.*, 2018, **11**(1), 64.
17 L. T. Senbanjo and M. A. Chellaiah, CD44: A Multifunctional Cell Surface Adhesion Receptor Is a Regulator of Progression and Metastasis of Cancer Cells, *Front. Cell Dev. Biol.*, 2017, **5**, 18.
18 M. Hassn Mesrati, S. E. Syafruddin, M. A. Mohtar and A. Syahir, CD44: A Multifunctional Mediator of Cancer Progression, *Biomolecules*, 2021, **11**(12), 1850.
19 S. Porcellini, C. Asperti, S. Corna, E. Cicoria, V. Valtolina, A. Stornaiuolo, B. Valentinis, C. Bordignon and C. Traversari, CAR T Cells Redirected to CD44v6 Control Tumor Growth in Lung and Ovary Adenocarcinoma Bearing Mice, *Front. Immunol.*, 2020, **11**, 99.
20 H. Son and A. Moon, Epithelial-mesenchymal Transition and Cell Invasion, *Toxicol. Res.*, 2010, **26**(4), 245–252.
21 J. Banyard and D. R. Bielenberg, The Role of EMT and MET in Cancer Dissemination, *Connect. Tissue Res.*, 2015, **56**(5), 403–413.
22 L. Isert, A. Mehta, G. Loiudice, A. Oliva, A. Roidl and O. M. Merkel, An In Vitro Approach to Model EMT in Breast Cancer, *Int. J. Mol. Sci.*, 2023, **24**(9), 7757.
23 M. A. Nieto, R. Y. Huang, R. A. Jackson and J. P. Thiery, EMT: 2016, *Cell*, 2016, **166**(1), 21–45.
24 M. Yilmaz and G. Christofori, EMT, the cytoskeleton, and cancer cell invasion, *Cancer Metastasis Rev.*, 2009, **28**(1), 15–33.
25 E. Olsson, G. Honeth, P.-O. Bendahl, L. H. Saal, S. Gruvberger-Saal, M. Ringnér, J. Vallon-Christersson, G. Jönsson, K. Holm, K. Lövgren, M. Fernö, D. Grabau, Å. Borg and C. Hegardt, CD44 isoforms are heterogeneously expressed in breast cancer and correlate with tumor subtypes and cancer stem cell markers, *BMC Cancer*, 2011, **11**(1), 418.
26 R. L. Brown, L. M. Reinke, M. S. Damerow, D. Perez, L. A. Chodosh, J. Yang and C. Cheng, CD44 splice isoform switching in human and mouse epithelium is essential for epithelial-mesenchymal transition and breast cancer progression, *J. Clin. Invest.*, 2011, **121**(3), 1064–1074.
27 R. A. Weinberg, *The Biology of Cancer*, 2014.
28 S. E. Leggett, A. M. Hruska, M. Guo and I. Y. Wong, The epithelial-mesenchymal transition and the cytoskeleton in bioengineered systems, *Cell Commun. Signaling*, 2021, **19**(1), 32.
29 W. Zhong, L. Pang, H. Feng, H. Dong, S. Wang, H. Cong, Y. Shen and Y. Bing, Recent advantage of hyaluronic acid for anti-cancer application: a review of "3S" transition approach, *Carbohydr. Polym.*, 2020, **238**, 116204.
30 Y. R. Zhang, R. Lin, H. J. Li, W. L. He, J. Z. Du and J. Wang, Strategies to improve tumor penetration of nanomedicines through nanoparticle design, *Wiley Interdiscip. Rev.: Nanomed. Nanobiotechnol.*, 2019, **11**(1), e1519.
31 G. Nabil and R. Alzhrani, CD44 Targeted Nanomaterials for Treatment of Triple-Negative Breast Cancer, *MDPI Cancers*, 2021, **13**(4), 898.
32 V. Hintze, M. Schnabelrauch and S. Rother, Chemical Modification of Hyaluronan and Their Biomedical Applications, *Front. Chem.*, 2022, **10**, 830671.
33 X. Chen, D. Iliopoulos, Q. Zhang, Q. Tang, M. B. Greenblatt, M. Hatziapostolou, E. Lim, W. L. Tam, M. Ni, Y. Chen, J. Mai, H. Shen, D. Z. Hu, S. Adoro, B. Hu, M. Song, C. Tan, M. D. Landis, M. Ferrari, S. J. Shin, M. Brown, J. C. Chang, X. S. Liu and L. H. Glimcher, XBP1 promotes triple-negative breast cancer by controlling the HIF1α pathway, *Nature*, 2014, **508**(7494), 103–107.
34 L. Isert, A. Mehta, F. Adams and O. M. Merkel, Tracking siRNA–Nanocarrier Assembly and Disassembly Using FRET, in *Quantitative Analysis of Cellular Drug Transport, Disposition, and Delivery*, ed. G. R. Rosania and G. M. Thurber, Springer US, New York, NY, 2021, pp. 383–396.
35 J. Hendrix, V. Baumgärtel, W. Schrimpf, S. Ivanchenko, M. A. Digman, E. Gratton, H. G. Kräusslich, B. Müller and D. C. Lamb, Live-cell observation of cytosolic HIV-1 assembly onset reveals RNA-interacting Gag oligomers, *J. Cell Biol.*, 2015, **210**(4), 629–646.
36 W. Schrimpf, A. Barth, J. Hendrix and D. C. Lamb, PAM: A Framework for Integrated Analysis of Imaging, Single-Molecule, and Ensemble Fluorescence Data, *Biophys. J.*, 2018, **114**(7), 1518–1528.
37 S. Ivanchenko and D. C. Lamb, in *Fluorescence Correlation Spectroscopy: Principles and Developments*, Supramolecular Structure and Function 10, Dordrecht, 2011, ed. J. Brnjas-Kraljević and G. Pifat-Mrzljak, Springer Netherlands, Dordrecht, 2011, pp. 1–30.
38 J. Schindelin, I. Arganda-Carreras, E. Frise, V. Kaynig, M. Longair, T. Pietzsch, S. Preibisch, C. Rueden, S. Saalfeld, B. Schmid, J.-Y. Tinevez, D. J. White, V. Hartenstein, K. Eliceiri, P. Tomancak and A. Cardona, Fiji: an open-source platform for biological-image analysis, *Nat. Methods*, 2012, **9**(7), 676–682.
39 S. Park, U. Han, D. Choi and J. Hong, Layer-by-layer assembled polymeric thin films as prospective drug delivery carriers: design and applications, *Biomater. Res.*, 2018, **22**(1), 29.
40 H. Wang, S. Zhang, J. Lv and Y. Cheng, Design of polymers for siRNA delivery: Recent progress and challenges, *View*, 2021, **2**(3), 20200026.
41 C. T. Greco, J. C. Andrechak, T. H. Epps and M. O. Sullivan, Anionic Polymer and Quantum Dot Excipients to Facilitate siRNA Release and Self-Reporting of Disassembly in Stimuli-Responsive Nanocarrier Formulations, *Biomacromolecules*, 2017, **18**(6), 1814–1824.
42 A. Tirella, K. Kloc-Muniak, L. Good, J. Ridden, M. Ashford, S. Puri and N. Tirelli, CD44 targeted delivery of siRNA by using HA-decorated nanotechnologies for KRAS silencing in cancer treatment, *Int. J. Pharm.*, 2019, **561**, 114–123.
43 Y. Yamada, M. Hashida and H. Harashima, Hyaluronic acid controls the uptake pathway and intracellular traffick-

ing of an octaarginine-modified gene vector in CD44 positive- and CD44 negative-cells, *Biomaterials*, 2015, **52**, 189–198.

44 M. Zhu, S. Perrett and G. Nie, Understanding the Particokinetics of Engineered Nanomaterials for Safe and Effective Therapeutic Applications, *Small*, 2013, **9**(9–10), 1619–1634.

45 D. Docter, U. Distler, W. Storck, J. Kuharev, D. Wünsch, A. Hahlbrock, S. K. Knauer, S. Tenzer and R. H. Stauber, Quantitative profiling of the protein coronas that form around nanoparticles, *Nat. Protoc.*, 2014, **9**(9), 2030–2044.

46 A. R. Petosa, D. P. Jaisi, I. R. Quevedo, M. Elimelech and N. Tufenkji, Aggregation and Deposition of Engineered Nanomaterials in Aquatic Environments: Role of Physicochemical Interactions, *Environ. Sci. Technol.*, 2010, **44(17)**, 6532–6549.

47 W. Richtering, I. Alberg and R. Zentel, Nanoparticles in the Biological Context: Surface Morphology and Protein Corona Formation, *Small*, 2020, **16**(39), 2002162.

48 S. Khan, A. Gupta and C. K. Nandi, Controlling the Fate of Protein Corona by Tuning Surface Properties of Nanoparticles, *J. Phys. Chem. Lett.*, 2013, **4(21)**, 3747–3752.

49 F. S. M. Tekie, M. Hajiramezanali, P. Geramifar, M. Raoufi, R. Dinarvand, M. Soleimani and F. Atyabi, Controlling evolution of protein corona: a prosperous approach to improve chitosan-based nanoparticle biodistribution and half-life, *Sci. Rep.*, 2020, **10**(1), 9664.

50 M. Bros, L. Nuhn, J. Simon, L. Moll, V. Mailänder, K. Landfester and S. Grabbe, The Protein Corona as a Confounding Variable of Nanoparticle-Mediated Targeted Vaccine Delivery, *Front. Immunol.*, 2018, **9**, 1760.

51 M. Suvarna, S. Dyawanapelly, B. Kansara, P. Dandekar and R. Jain, Understanding the Stability of Nanoparticle–Protein Interactions: Effect of Particle Size on Adsorption, Conformation and Thermodynamic Properties of Serum Albumin Proteins, *ACS Appl. Nano Mater.*, 2018, **1(10)**, 5524–5535.

52 J. J. Green, E. Chiu, E. S. Leshchiner, J. Shi, R. Langer and D. G. Anderson, Electrostatic Ligand Coatings of Nanoparticles Enable Ligand-Specific Gene Delivery to Human Primary Cells, *Nano Lett.*, 2007, **7**(4), 874–879.

53 L. Nuhn, M. Hirsch, B. Krieg, K. Koynov, K. Fischer, M. Schmidt, M. Helm and R. Zentel, Cationic Nanohydrogel Particles as Potential siRNA Carriers for Cellular Delivery, *ACS Nano*, 2012, **6**(3), 2198–2214.

54 S. Schmitt, A. Huppertsberg, A. Klefenz, L. Kaps, V. Mailänder, D. Schuppan, H.-J. Butt, L. Nuhn and K. Koynov, Fluorescence Correlation Spectroscopy Monitors the Fate of Degradable Nanocarriers in the Blood Stream, *Biomacromolecules*, 2022, **23**(3), 1065–1074.

55 O. M. Merkel, D. Librizzi, A. Pfestroff, T. Schurrat, K. Buyens, N. N. Sanders, S. C. De Smedt, M. Behe and T. Kissel, Stability of siRNA polyplexes from poly(ethylenimine) and poly(ethylenimine)-g-poly(ethylene glycol) under in vivo conditions: effects on pharmacokinetics and biodistribution measured by Fluorescence Fluctuation Spectroscopy and Single Photon Emission Computed Tomography (SPECT) imaging, *J. Controlled Release*, 2009, **138**(2), 148–159.

56 B. M. Cooper and D. Putnam, Polymers for siRNA Delivery: A Critical Assessment of Current Technology Prospects for Clinical Application, *ACS Biomater. Sci. Eng.*, 2016, **2**(11), 1837–1850.

57 B. Naeye, H. Deschout, V. Caveliers, B. Descamps, K. Braeckmans, C. Vanhove, J. Demeester, T. Lahoutte, S. C. De Smedt and K. Raemdonck, In vivo disassembly of IV administered siRNA matrix nanoparticles at the renal filtration barrier, *Biomaterials*, 2013, **34**(9), 2350–2358.

58 M. Zheng, D. Librizzi, A. Kılıç, Y. Liu, H. Renz, O. M. Merkel and T. Kissel, Enhancing in vivo circulation and siRNA delivery with biodegradable polyethylenimine-graft-polycaprolactone-block-poly(ethylene glycol) copolymers, *Biomaterials*, 2012, **33**(27), 6551–6558.

59 I. S. Bayer, Hyaluronic Acid and Controlled Release: A Review, *Molecules*, 2020, **25**(11), 2649.

60 L. Zhong, L. Xu, Y. Liu, Q. Li, D. Zhao, Z. Li, H. Zhang, H. Zhang, Q. Kan, Y. Wang, J. Sun and Z. He, Transformative hyaluronic acid-based active targeting supramolecular nanoplatform improves long circulation and enhances cellular uptake in cancer therapy, *Acta Pharm. Sin. B*, 2019, **9**(2), 397–409.

61 M. B. Parmar, D. N. Meenakshi Sundaram, K. C. Remant Bahadur, R. Maranchuk, H. Montazeri Aliabadi, J. C. Hugh, R. Löbenberg and H. Uludağ, Combinational siRNA delivery using hyaluronic acid modified amphiphilic polyplexes against cell cycle and phosphatase proteins to inhibit growth and migration of triple-negative breast cancer cells, *Acta Biomater.*, 2018, **66**, 294–309.

62 A. Almalik, R. Donno, C. J. Cadman, F. Cellesi, P. J. Day and N. Tirelli, Hyaluronic acid-coated chitosan nanoparticles: molecular weight-dependent effects on morphology and hyaluronic acid presentation, *J. Controlled Release*, 2013, **172**(3), 1142–1150.

63 P. Kesharwani, R. Chadar, A. Sheikh, W. Y. Rizg and A. Y. Safhi, CD44-Targeted Nanocarrier for Cancer Therapy, *Front. Pharmacol.*, 2022, **12**, 800481.

64 J. A. Hinneh, J. L. Gillis, N. L. Moore, L. M. Butler and M. M. Centenera, The role of RHAMM in cancer: Exposing novel therapeutic vulnerabilities, *Front. Oncol.*, 2022, **12**, 982231.

65 A. Spadea, J. M. Rios de la Rosa, A. Tirella, M. B. Ashford, K. J. Williams, I. J. Stratford, N. Tirelli and M. Mehibel, Evaluating the Efficiency of Hyaluronic Acid for Tumor Targeting via CD44, *Mol. Pharm.*, 2019, **16**(6), 2481–2493.

66 A. Almalik, S. Karimi, S. Ouasti, R. Donno, C. Wandrey, P. J. Day and N. Tirelli, Hyaluronic acid (HA) presentation as a tool to modulate and control the receptor-mediated uptake of HA-coated nanoparticles, *Biomaterials*, 2013, **34**(21), 5369–5380.

67 S. Bolte and F. P. Cordelières, A guided tour into subcellular colocalization analysis in light microscopy, *J. Microsc.*, 2006, **224**(3), 213–232.

 

68 A. M. Moreno-Echeverri, E. Susnik, D. Vanhecke, P. Taladriz-Blanco, S. Balog, A. Petri-Fink and B. Rothen-Rutishauser, Pitfalls in methods to study colocalization of nanoparticles in mouse macrophage lysosomes, *J. Nanobiotechnol.*, 2022, **20**(1), 464.

69 E. A. Pérez-Yépez, J.-T. Ayala-Sumuano, A. M. Reveles-Espinoza and I. Meza, Selection of a MCF-7 Breast Cancer Cell Subpopulation with High Sensitivity to IL-1β: Characterization of and Correlation between Morphological and Molecular Changes Leading to Increased Invasiveness, *Int. J. Breast Cancer*, 2012, **2012**, 609148.

70 L. Li, Y. Zhang and J. Wang, Effects of ligand distribution on receptor-diffusion-mediated cellular uptake of nanoparticles, *R. Soc. Open Sci.*, 2017, **4**(5), 170063.

71 A. Albanese and W. C. Chan, Effect of gold nanoparticle aggregation on cell uptake and toxicity, *ACS Nano*, 2011, **5**(7), 5478–5489.

72 A. Bandyopadhyay, R. L. Fine, S. Demento, L. K. Bockenstedt and T. M. Fahmy, The impact of nanoparticle ligand density on dendritic-cell targeted vaccines, *Biomaterials*, 2011, **32**(11), 3094–3105.

73 S. Ouasti, P. J. Kingham, G. Terenghi and N. Tirelli, The CD44/integrins interplay and the significance of receptor binding and re-presentation in the uptake of RGD-functionalized hyaluronic acid, *Biomaterials*, 2012, **33**(4), 1120–1134.

74 N. M. Zaki, A. Nasti and N. Tirelli, Nanocarriers for Cytoplasmic Delivery: Cellular Uptake and Intracellular Fate of Chitosan and Hyaluronic Acid-Coated Chitosan Nanoparticles in a Phagocytic Cell Model, *Macromol. Biosci.*, 2011, **11**(12), 1747–1760.

75 H. Li, X. Chen, Y. Gao, J. Wu, F. Zeng and F. Song, XBP1 induces snail expression to promote epithelial- to-mesenchymal transition and invasion of breast cancer cells, *Cell. Signalling*, 2015, **27**(1), 82–89.

76 W. Shi, Z. Chen, L. Li, H. Liu, R. Zhang, Q. Cheng, D. Xu and L. Wu, Unravel the molecular mechanism of XBP1 in regulating the biology of cancer cells, *J. Cancer*, 2019, **10**(9), 2035–2046.

77 S. Chen, J. Chen, X. Hua, Y. Sun, R. Cui, J. Sha and X. Zhu, The emerging role of XBP1 in cancer, *Biomed. Pharmacother.*, 2020, **127**, 110069.

78 L. Isert, M. Passi, B. Freystetter, M. Grab, A. Roidl, C. Muller, A. Mehta, H. G. Sundararaghavan, S. Zahler and O. M. Merkel, Cellular EMT-status governs contact guidance in an electrospun TACS-mimicking in vitro model, *Mater. Today Bio*, 2025, **30**, 101401.